

Master thesis and internship[BR]- Master's thesis : Simulation of a wingtip vortex flow with Linear Eddie Viscosity turbulence models at $Re = 4.6E6$ and $Re = 1.2E6$ [BR]- Integration Internship

Auteur : Tonioni, Niccolò

Promoteur(s) : Terrapon, Vincent

Faculté : Faculté des Sciences appliquées

Diplôme : Master en ingénieur civil en aérospatiale, à finalité spécialisée en "aerospace engineering"

Année académique : 2021-2022

URI/URL : <http://hdl.handle.net/2268.2/16121>

Avertissement à l'attention des usagers :

Tous les documents placés en accès ouvert sur le site le site MatheO sont protégés par le droit d'auteur. Conformément aux principes énoncés par la "Budapest Open Access Initiative"(BOAI, 2002), l'utilisateur du site peut lire, télécharger, copier, transmettre, imprimer, chercher ou faire un lien vers le texte intégral de ces documents, les disséquer pour les indexer, s'en servir de données pour un logiciel, ou s'en servir à toute autre fin légale (ou prévue par la réglementation relative au droit d'auteur). Toute utilisation du document à des fins commerciales est strictement interdite.

Par ailleurs, l'utilisateur s'engage à respecter les droits moraux de l'auteur, principalement le droit à l'intégrité de l'oeuvre et le droit de paternité et ce dans toute utilisation que l'utilisateur entreprend. Ainsi, à titre d'exemple, lorsqu'il reproduira un document par extrait ou dans son intégralité, l'utilisateur citera de manière complète les sources telles que mentionnées ci-dessus. Toute utilisation non explicitement autorisée ci-avant (telle que par exemple, la modification du document ou son résumé) nécessite l'autorisation préalable et expresse des auteurs ou de leurs ayants droit.

Simulation of a wingtip vortex flow with Linear Eddie Viscosity turbulence models at $Re = 4.6E6$ and $Re = 1.2E6$

University of Liège - School of Engineering and Computer Science
Politecnico di Milano - School of Aeronautical Engineering

Master's thesis completed in order to obtain the degree of Master of Science in Aerospace Engineering

Academic year 2021-2022

Supervisors: A. Abbà, K. Hillewaert, V. Terrapon

Niccolò Tonioni

Acknowledgments

The present research benefited from computational resources made available on the Tier-1 supercomputer of the Fédération Wallonie-Bruxelles, infrastructure funded by the Walloon Region under the grant agreement n°1117545, and from the ones provided by the Consortium des Équipements de Calcul Intensif (CÉCI), funded by the Fonds de la Recherche Scientifique de Belgique (F.R.S.-FNRS) under Grant No. 2.5020.11 and by the Walloon Region.

I would also like to thank my supervisors, who followed me during the entire project and spent a significant amount of time helping me.

*Niccolò Tonioni
ULiège, Polimi, August 2022*

Contents

Acknowledgments	ii
1 Introduction	1
2 Theoretical background	3
2.1 Turbulence models	3
2.1.1 Large Eddie Simulations	5
2.1.2 Discontinuous Galerkin Method	7
2.1.3 Reynolds Average Navier-Stokes equations	9
3 Flow Description and Computational Setup	12
3.1 Computational domain	12
3.2 Boundary conditions	14
3.2.1 RANS boundary conditions	14
3.2.2 LES boundary and initial conditions	14
3.3 Numerical schemes	15
3.3.1 SU2 solver	15
3.3.2 ARGO solver	15
3.4 Mesh generation	16
3.4.1 RANS mesh	16
3.4.2 LES mesh	17
4 Results and discussion	21
4.1 Wing surface	21
4.1.1 Skin friction field	21
4.1.2 Pressure field	27
4.2 Vortex formation and propagation	31
4.2.1 Vortex centerline identification	31
4.2.2 Vortex centerline mean quantities evolution	35
4.2.3 Vortex development in the near wake	37
4.3 Reynolds stress evolution in the near wake vortex	37
4.4 LES computations	46
5 Further discussion and future work indications	48
6 Conclusion	50
References	52

1

Introduction

Turbulence modeling has become an essential aspect of many engineering devices' performances. In combustion chambers, turbulence increases fuel/air mixing, reducing emissions; in wind turbine design, the knowledge of the turbulence in the incoming flow and the blades' boundary layer is essential to increase their energy production. In nautical design, delaying the occurrence of turbulence in boundary layers over the foil surfaces improve aerodynamic efficiency; in Formula 1 cars design, the generation and control of turbulent flow features such as wakes and highly vortical structures are vital to increase the car performance. There is, therefore, a significant demand for new techniques to simulate, predict, and analyze turbulent flows. However, the representation of these turbulent motions is very challenging due to significant and irregular variations of the fluid velocity field both in position and time and the additional practical needs of numerical stability and computational efficiency. Therefore, even the most complicated models need radically simplifying assumptions about the structure of the underlying turbulence.

In this context, Computational Fluid Dynamics (CFD) analyses have become an essential tool for several practical and industrial problems. Analysis of turbulent flows using Direct Numerical Simulation (DNS) and Large-Eddy Simulations (LES) started almost sixty years ago, with the pioneering work of Smagorinsky in 1963 [39]. Over the past half-century, they have more and more supplemented experimental measurements, fostered by continuous computer power growth. Nevertheless, the Reynolds average Navier-Stokes (RANS) models are still the most widely used methods in academia and industry. These rely entirely on modeling assumptions to represent turbulent characteristics, leading to lower computational requirements. Moreover, their solutions directly provide the mean flow, making them computationally very tractable and appealing for engineering applications.

Although new and increasingly complex models are being developed [52, 28], most of the RANS methods used in industrial and academic CFD solvers were formulated and published in the 1980s, and 1990s [6, 51]. Surprisingly the hypothesis at the heart of these models dates a century before, when J. Boussinesq postulated a linear relationship between Reynolds stresses and mean strain rate tensors, twenty years before Reynolds stresses were even formulated [3]. The averaged equations are then closed by defining a scalar constant, determining the proportionality between the two tensors, with independent turbulent quantities, computed with additional transport equations. These closure models are called Linear Eddy Viscosity Models (LEVM). It is essential to notice that Boussinesq's assumption is a strong hypothesis, which does not hold in many engineering-relevant flows, such as those with curvature, impingement, and separation [4]. Even for simple shear flows, it cannot capture the anisotropic nature of the Reynold stresses. Accuracy is, therefore, a critical aspect of LEVM.

A classical approach to predict these models' success or failure has relied on domain expertise and statistical data analysis, possibly switching to more sophisticated closures or high fidelity large-eddy simulations. However, the recent dramatic improvement in modern machine learning (ML) strategies has brought a fresh perspective to the problem. Several authors used ML to identify and model Reynold stress tensor discrepancies between RANS simulation and high-fidelity data. Ling and Templeton [20] compared support-vector machines, Adaboost decision trees, and random forests to classify and predict high-uncertainty regions in the Reynold stress tensor. Parish and Duraisany [12] used an ML framework and field inversion to build corrective models based on inverse problems. Singh et al. [38] later

used these models to develop a neural-network enhanced correction for the Spalart-Allmaras model. Ling et al. [21] developed a deep neural network architecture to model the anisotropic Reynolds-stress tensor, based on the tensor polynomial decomposition proposed by Pope [30]. This architecture's novel characteristic is that it incorporates a multiplicative layer to embed Galileian invariance in the tensor predictions.

This work aims to study the accuracy of RANS simulations in the formation and evolution of a wingtip vortex to identify potential approaches to improve Boussinesq's hypothesis using an ML framework. This flow type was chosen because of its modeling complexity and relevance in many practical industrial applications. The development and interactions of the primary and secondary vortices generated by the wing cap, combined with the high curvature of the streamlines and the high velocity and pressure gradients in all three directions, make it particularly challenging to model. Nevertheless, the characterization of the vortical structures shed from lifting surfaces is of primary importance on wind turbines, helicopter blades, propeller cavitation in ships, high-lift configurations of aircraft, and the high-performance automotive industry [2, 34, 33].

This project's initial objective was to compute and compare LES and RANS simulations of the three-dimensional turbulent flow over a NACA-0012 half wing mounted at the wall to study the accuracy of LEVM on wingtip vortex, and identify input and output variables to be used in an ML-based model. However, due to the setup of the simulations and the computing time requirements, we failed to obtain LES simulations of the full wing. Therefore, we decided to compare the results obtained with a Negative Spalart-Allmaras [1] and a Menter's Shear Stress Transport turbulent models [25] with the experimental data proposed by Chow et al. [7] and the RANS simulations of Churchfield et al. [8] at a free stream Reynolds number $Re = 4.3 \times 10^6$ and Mach number $M = 0.14$. Furthermore, we studied the effects of the Reynolds number performing the same simulations at $Re = 1.2 \times 10^6$, comparing with the LES results of Lombard et al. [23]. To solve the RANS equations, we use the open source software SU2 [43].

In Chap.2 we present a theoretical background of turbulence models, providing an overview of the main challenges and differences between LES and RANS modeling. Chap.3 reports a description of the flow investigated and the computational setup defined for the simulations. In Chap.4 we analyze the results obtained with the RANS simulations by comparing them with the reference results. Moreover, we present a qualitative overview of the instantaneous flow computed with implicit LES simulations on the wing airfoil profile extruded in the third direction with periodic span-wise boundary conditions. The latter can be helpful in the future development of the work to improve the mesh refinements. Chap.5 is dedicated to discussing future work to enhance turbulence closure using supervised learning methods, starting from what was observed in the results.

2

Theoretical background

Turbulence is one of the last unsolved problems of classical physics. Although it can be defined using physical laws, its description is challenging due to its non-linear, multiscale, chaotic nature. Nevertheless, turbulence phenomena play key roles in many practical engineering problems. Engineers rely on turbulence models to study these complex flows, trying to find the best compromise between an accurate description of the physics and computational efficiency.

2.1. Turbulence models

In a continuum mechanic framework, the Navier-Stokes equations, complemented by the thermodynamic equation for the fluid state and empirical laws for the diffusion coefficients dependency on the other variables, represent a complete mathematical model to study turbulent flows. The solution is obtained numerically using Partial Differential Equations (PDE) algorithms. A first intuitive approach is directly applying those algorithms to the unsteady Navier-Stokes equations (DNS). However, one would need to resolve all the physical flow's space-time scales, equivalent to requiring the numerical result's space-time resolution scale to be as refined as the continuous problem one. This can be extremely constrictive in the case of turbulence, characterized by scales of very different sizes. Researchers have developed LES and RANS models to overcome this limit. These methods decrease the computational cost by solving the equation at a coarser level of the fluid system description.

To better understand the multiscale nature of turbulence and the differences in DNS, LES, and RANS models, we firstly review the basic concepts of Richardson's *energy cascade* and *Kolmogorov hypotheses*. In Richardson's view, turbulence is considered a sea of eddies of different sizes. An 'eddy' eludes a precise definition. It can be seen as a region of the flow of size l , characterized by a turbulent motion, which is at least moderately coherent over this area. Besides having a characteristic size, each eddy is associated with a velocity $u(l)$ and a timescale $\tau(l)$.

A length l_0 , comparable to the flow scale L , characterize the eddies in the largest scales. Their characteristic velocity $u(l_0)$ is in the order of the root mean square turbulence velocity fluctuations $u' = (\frac{2}{3}k)^{1/2}$, comparable to u_L , the characteristic flow velocity. The Reynolds number of these eddies is therefore comparable to the one of the flow (i.e., is large), so direct effects of the viscosity are negligible. Richardson theorizes that these large eddies, created by the mean flow, are unstable and break up into smaller eddies, transferring their energy to them. Then the process continues until the Reynolds number $Re = u(l)l/\nu$ is sufficiently small that the eddy motion is stable, and molecular viscosity effectively dissipates the kinetic energy. Kolmogorov added to this theory, formulating hypotheses that help quantify and characterize these different scales.

Local isotropy hypothesis: At sufficiently high Reynolds numbers, the small-scale turbulent motions ($\eta = l \ll l_0$) are statistically isotropic.

First similarity hypothesis: At sufficiently high Reynolds numbers, the statistic of small-scale motions has a universal form that is uniquely determined by the molecular viscosity ν and the rate of dissipation ϵ .

Second similarity hypothesis: At sufficiently high Reynolds numbers, the statistic of the motions of the length scale l , with $\eta \ll l \ll l_0$, have a universal form uniquely determined by the rate of dissipation ϵ .

These hypotheses define three length scale ranges: an energy-containing range and a universal equilibrium range, divided into an inertial sub-range ($l_{DI} < l < l_{EI}$) and a dissipation range ($l < l_{DI}$). The suffixes EI and DI stand for the demarcation between the energy range (E) and the inertial sub-range (I) and between the inertial sub-range and the dissipation range (D). An illustration of these different scales and the energy distribution within them is presented in Fig.2.1. The energy bulk is contained in the larger eddies and is transferred to the smaller ones via the inertial sub-range. In the smaller scales, all the directional bias of the larger scales is lost (local isotropy hypothesis). The length η , the velocity u_η and time τ_η , characterizing these scales, can be uniquely defined by the dissipation rate ϵ and the molecular viscosity ν (first similarity hypothesis). In the inertial sub-range, the viscous effects are negligible, and inertial effects determine the motions (second similarity hypothesis). A central point in this formulation is that the rate of energy transfer $\mathcal{T}(l)$ to the smaller scales balances the dissipation rate, i.e., $\mathcal{T}(l) \approx \epsilon$. That is, the rate of transfer from the larger scales determines the constant rate of energy transfer to the inertial sub-range, hence the dissipation rate. Or, from a modeling perspective, a correct definition or modeling of the smaller scales is needed to correctly represent the larger structures of turbulence, which are the ones of interest.

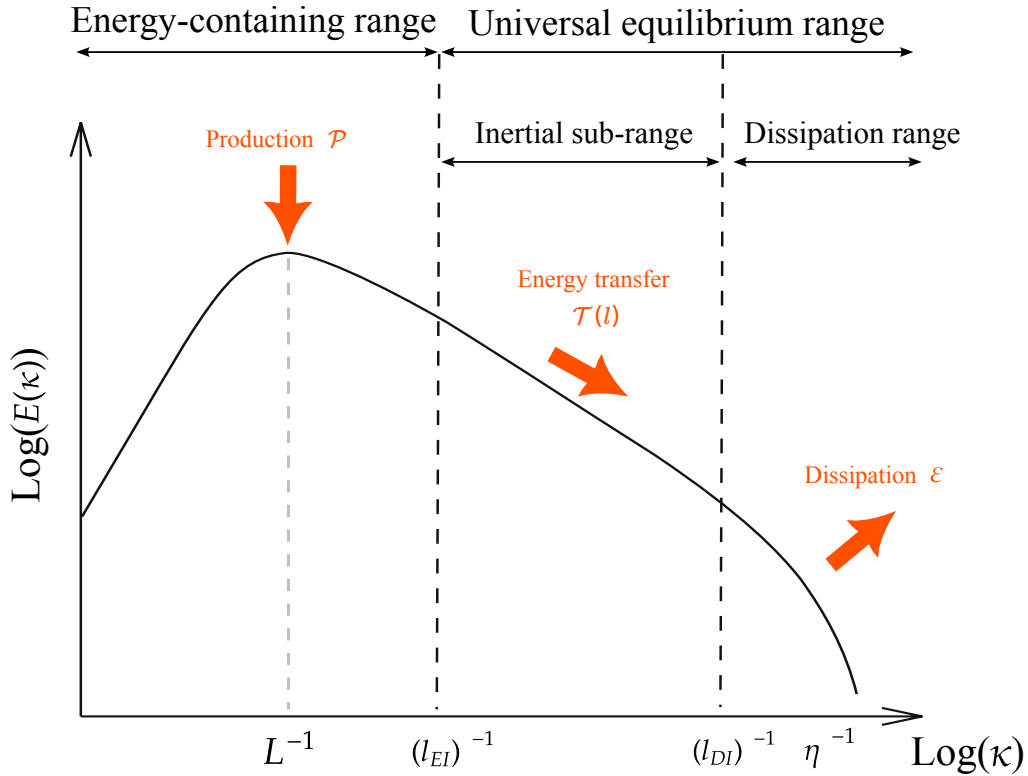


Figure 2.1: Illustration of the energy spectrum for homogeneous isotropic turbulence at high Reynolds number. In the center of the wave number range, the curve exhibit power-law behavior defined by the Kolmogorov -5/3 law, i.e., $E(\kappa) = C_\kappa \epsilon^{2/3} \kappa^{-5/3}$, where C_κ is a constant. Common values for l_{EI} and l_{DI} are $L/6$ and 60η , respectively.

To illustrate the critical issues in resolving all the physical flow's space-time scales, let us consider statistically homogeneous and isotropic turbulence. For this type of flow, the Kolmogorov hypothesis allows for a quantification of the ratio between the larger and the smaller scales:

$$\begin{aligned} \frac{L}{\eta} &= \mathcal{O}\left(Re^{3/4}\right) \\ \frac{\tau_L}{\tau_\eta} &= \mathcal{O}\left(Re^{1/2}\right) \end{aligned} \tag{2.1}$$

Therefore for three-dimensional space, $\mathcal{O}(Re^{9/4})$ degrees of freedom are needed to represent all the spatial flow scales. Even if the time ratio varies as $\mathcal{O}(Re^{1/2})$, the use of an explicit time-integration algorithm leads to a linear dependency of the time step to the mesh size. Therefore a Direct Numerical Simulation would require solving the Navier-Stokes equations $\mathcal{O}(Re^3)$ times to calculate the evolution of the solution for a duration equal to the characteristic time of the most energetic scale. Aeronautical applications usually deal with large Reynolds numbers (it can reach up to 10^8). Therefore the computational requirements would be greater than the resources currently available. To compute the solution, more tractable models, obtained by introducing a coarser flow system description level, are defined. Fig.2.2 illustrates an example of this concept. Large eddy simulations reduce the number of degrees of freedom of the numerical solution by projecting the solution on an ad-hoc function basis and solving only the low-frequency modes in space. Reynolds Average Navier Stokes models directly compute the solution's statistical average. Here the statistical character of the solution prevents a fine description of physical mechanisms.

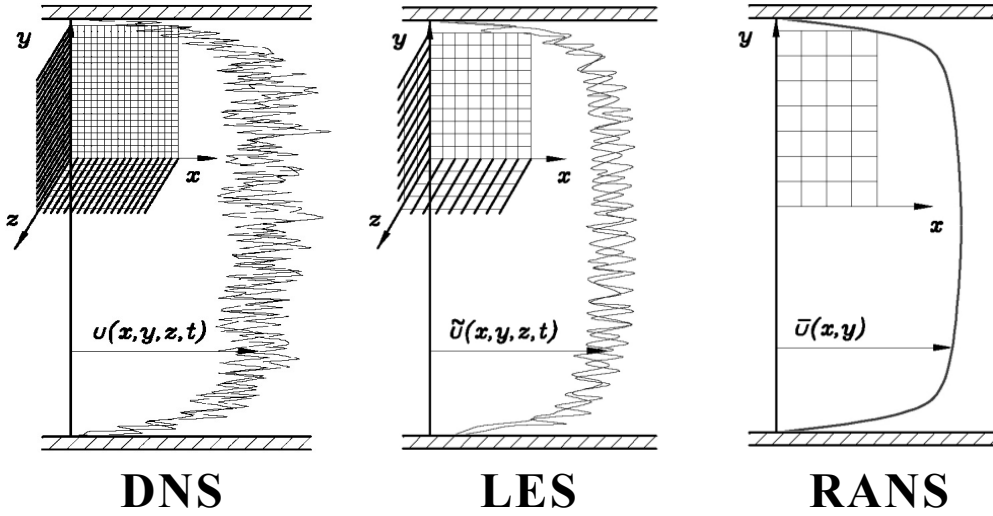


Figure 2.2: Different levels of spatial description for a DNS, LES and RANS channel flow simulation. Adapted from [45].

As illustrated by the energy cascade concept, a dynamic coupling exists between all the scales (mathematically represented by the non-linearity of the Navier-Stokes equation). Therefore, the correct representation of the solved scales is obtained only by correctly modeling the non-solved scales' interactions by introducing statistical models that reflect the global or average actions. These will be further discussed in Sec.2.1.1 and 2.1.3.

2.1.1. Large Eddy Simulations

LES formulation aims to reduce the computational cost by solving the equations in a coarser computational grid. As learned from the Kolmogorov theory, the larger energy-containing scales are directly affected by the flow geometry and thus are the ones of interest. On the contrary, the smaller scales have, to some extent, a universal character. When resolving in a coarser grid, the method cannot describe the smaller turbulent motions (sub-grid scales). As a result, these will be cut off from the solution, as shown in Fig.2.3. To still solve the larger motions, the LES formulation must correctly represent the interaction between the larger and smaller scales, which implies accurately expressing the energy transfer rate at the inertial sub-range.

Because large-eddy simulation implies unresolved energy, two essential points must be considered. The method must avoid non-linear aliasing (accurately representing energy transfer and destruction) and correctly describe backscatter (inverse energy transfer from small to large scales). Two primary ways are identified to address these criticalities: the *explicit* large eddy simulations approach and the *implicit* approach.

In an explicit approach the velocity $\mathbf{U}(\mathbf{x}, t)$ is decomposed into the sum of a filtered (resolved) component $\bar{\mathbf{U}}(\mathbf{x}, t)$ and a residual (sub-grid scale) component $\mathbf{u}'(\mathbf{x}, t)$. The filtered velocity $\bar{\mathbf{U}}(\mathbf{x}, t)$ represents the three dimensional and time-dependent motion of the large eddies, the new unknown. The equa-

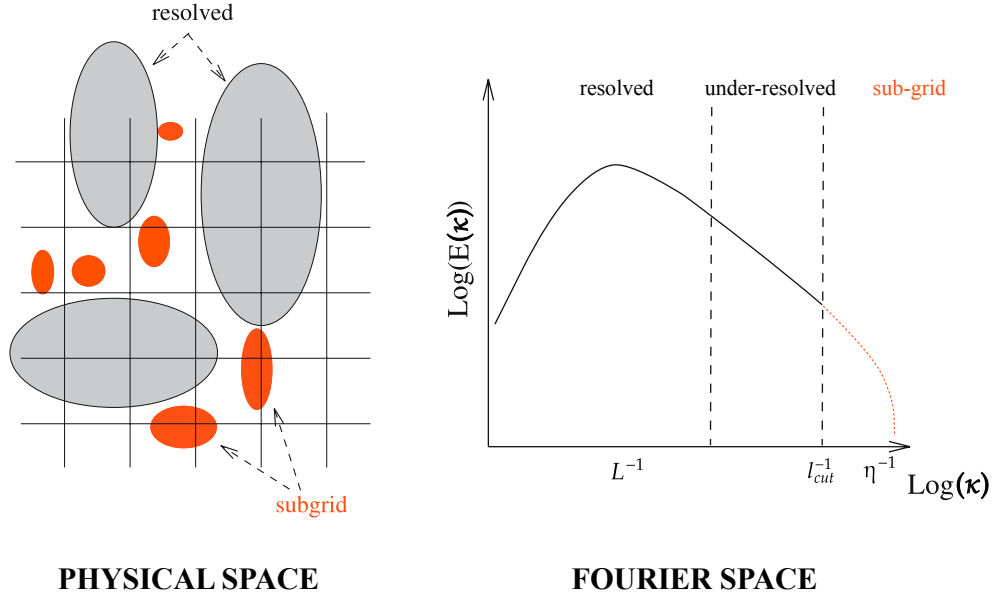


Figure 2.3: Illustration of large eddy simulations resolved and cut-off scales in the physical and Fourier space. Three zones can be defined: the resolved range, corresponding to the larger scales, an under-resolved or sacrificed range, and a sub-grid range, corresponding to the smaller scales. The cut frequency demarcates the separation between the frequencies present in the numerical solution and those that are not. For an LES solution, it is usually placed where the scales start to show self-similarity (dissipation repeats itself at different scales).

tions for its evolution are derived from the Navier-Stokes equations through a filtering operation and then are solved numerically. This operation can be defined in different ways depending on the model. The most common is to express the low-pass filter as a convolution product. The derived equations contain an un-closed term in the momentum equation: the sub-grid tensor (or residual stress tensor), which arises from the non-linear term of the Navier-Stokes equations. The closure is obtained by introducing a model for it, which must provide turbulent synchronization (avoid aliasing) and catch the effect of the smaller scales on the larger ones (backscatter). Because the equations are solved numerically, alongside the modeling definition, one should consider the numerical method choice. There are two viewpoints to this end: in one, the filter and model are identified independently of the numerical method, which implies independently of the grid employed. Hence, the dispersion and dissipation errors of the numerical method are supposed to be low enough to provide an accurate solution to the filtered equations. The alternative point of view is that modeling and numerical issues should be combined. In practice, the two are interwoven to some extent.

In an implicit approach, no filtering is introduced. The unsteady Navier-Stokes equations are numerically solved on a coarser grid by projecting the solution on an ad-hoc function basis. The solution physics entirely depends on the numerical method. Its dissipation is directly used to model the sub-grid dissipation rate, such that the model predicts an accurate rate of energy transfer. Therefore, the dissipation and dispersion errors of the numerical method directly affect the energy spectrum and the convective terms, respectively. For these reasons, the choice of the numerical scheme has significant importance. Low-order schemes are usually inadequate due to high numerical dispersion and dissipation. High-order schemes reduce the dissipation localizing it at higher frequencies of the energy spectrum and decrease the numerical dispersion, accurately representing the turbulent convection. The Discontinuous Galerkin method (DGM) is a well-suited candidate for developing an implicit LES approach because they allow for higher order scheme formulation in a finite element framework.

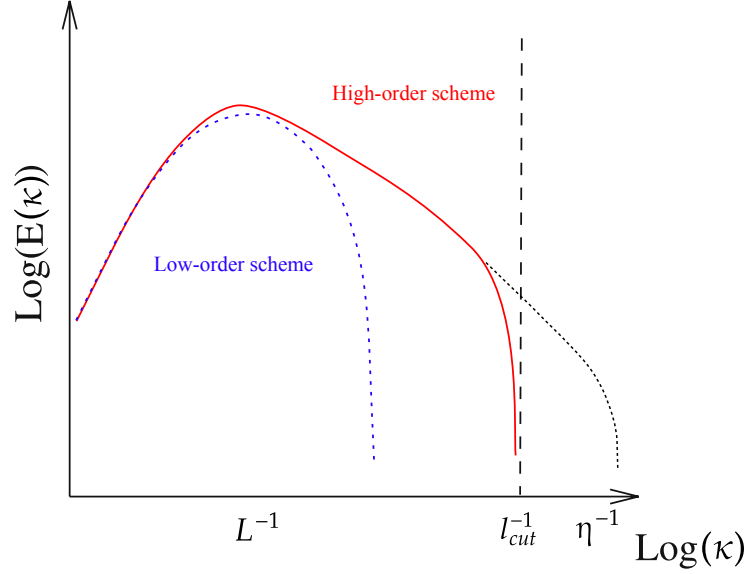


Figure 2.4: Illustration of the energy spectrum modeled by different numerical schemes. Low-order schemes introduce numerical dissipation at a broader range of frequencies, resulting in a non-physical description of the energy spectrum, thus of the larger turbulent motions. Instead, high-order schemes accurately represent the inertial sub-range slope (directly linked to the energy transfer and dissipation) by adding numerical dissipation only to the higher frequencies of the spectrum.

2.1.2. Discontinuous Galerkin Method

DGM is a finite element method (FEM), which uses a discontinuous interpolation combined with a Galerkin variational formulation. Considering a general system of N coupled convection-diffusion-source equations in *conservative* form, defined in a D dimensional domain Ω :

$$\frac{\partial q_m}{\partial t} + \nabla \cdot \mathbf{f}_m + \nabla \cdot \mathbf{d}_m + s_m = 0, \quad \forall q_m \in \mathcal{U} \quad (2.2)$$

where the subscript index $m = 1, \dots, N$ corresponds to a variable, q represent the conserved variables, $\mathbf{f} \in \mathcal{U}^{N \times D}$ the convective flux vector, $\mathbf{d} \in \mathcal{U}^{N \times D}$ the diffusive flux vector, and $s \in \mathcal{U}^N$ the source term. FEM is based upon a mesh (or grid), which approximates the domain Ω by a collection of simple geometrical elements e :

$$\lim_{h \rightarrow 0} \Omega_h = \Omega, \quad \Omega_h = \cup_e e \quad (2.3)$$

where h is the characteristic mesh size. The solution space \mathcal{U}^N of Eq.2.2 is then approximated using the grid as a support, such that:

$$\lim_{h \rightarrow 0} \mathcal{U}_h^N = \mathcal{U}^N \quad (2.4)$$

where \mathcal{U}_h^N is called the trial space. The terms \tilde{u}_m of the solution state vector $\tilde{u} \in \mathcal{U}^N$ are expressed as the linear combination of shape functions ϕ_j , which constitute a suitable set of basis functions for \mathcal{U}_h :

$$\tilde{u}_m \approx u_m = u_{mi} \phi_i \quad \mathcal{U}_h = \text{span} \{ \phi_j, j \in [0, U] \} \quad (2.5)$$

The scalars u_{mi} represent the expansion weights associated with the variable m with respect to the i -th shape function ϕ_i . In the trial space \mathcal{U}_h^N these basis are chosen as the columns of the matrix $\phi = (\phi_{11} \ \phi_{12} \ \dots \ \phi_{1U} \ \dots \ \phi_{N1} \ \phi_{N2} \ \dots \ \phi_{NU})$. We can therefore rewrite the solution as:

$$u = u_{mi} \phi_{mi}. \quad (2.6)$$

Since the solution is approximated, Eq.2.2 can not be satisfied everywhere in the domain. Therefore the equations are re-defined using the weak formulation as a Galerkin Variational problem, which requires the equations residual to be orthogonal to all members v of a test space $\mathcal{V}_e^N = \mathcal{U}_h^N$.

$$\mathcal{L}(u, v) = \int_{\Omega} v \left(\frac{\partial q}{\partial t} + \nabla \cdot \mathbf{f} + \nabla \cdot \mathbf{d} + s \right) dV = 0, \quad \forall v \in \mathcal{U}_h^N \quad (2.7)$$

where the sum over the variable index m is implied and the test functions v can also be expressed as linear combinations of the same basis used for u .

$$v = v_{mi} \phi_{mi} \quad (2.8)$$

Using this framework, Discontinuous Galerkin methods define Eq.2.7 by choosing as trial space a *broken* vectorial space (often polynomial). Its elements consist of vectors of functions that are fully regular within each mesh element but not necessarily continuous across elements. These guarantee DGM greater freedom of shape function choice than the classical continuous FEM. The possibility of being discontinuous across elements makes the shape function construction easy and flexible: any shape function can be supported on a single element, and the interpolation can change from element to element (usually the order). Another significant difference between the DG and continuous FE methods is the presence of additional terms in the Galerkin variational formulation, arising from the element boundary fluxes. Using a Discontinuous Galerkin formulation Eq.2.7 is rewritten as follow:

$$\sum_e \int_e v \frac{\partial q}{\partial t} dV + \sum_e \int_e \nabla v \cdot \mathbf{h} dV + \sum_e \int_e v s dV + \sum_f \int_f \gamma(u^+, u^-; v^+, v^-; \mathbf{n}) dS = 0, \quad \forall v \in \mathcal{U}_h^N \quad (2.9)$$

where f represent the element faces, \mathbf{h} stand for \mathbf{f} or \mathbf{g} or their sum, \mathbf{n} the normal direction to the element boundary (for each element $+$ symbol define the outward pointing normal, while $-$ the opposite direction), and γ is the *interface flux*. For consistency the latter should be chosen such that for a continuous solution $u^+ = u^- = \tilde{u}$, and $\mathbf{h}(u^+) = \mathbf{h}(u^-)$, the following relation is satisfied:

$$\gamma(u^+, u^-; v^+, v^-; \mathbf{n}) = \llbracket v \rrbracket \cdot \mathbf{h}(\tilde{u}). \quad (2.10)$$

where $\llbracket \cdot \rrbracket$ define the jump operator $\llbracket x \rrbracket = x^+ \mathbf{n}^+ + x^- \mathbf{n}^-$.

Eq.2.9 provides a general derivation of the Discontinuous Galerkin formulation. The user have great freedom in the flux function $\gamma(u^+, u^-; v^+, v^-; \mathbf{n})$ choice. We will now give a brief overview of how this term can be treated to assure stability in the case of convective and diffusive fluxes.

Considering the hyperbolic subsystem, DGM can be interpreted as an extension of first-order Finite Volume Methods (FVM) to high-order [18]. FVM uses the integral form of the convection equations to compute the cell average evolution of the conservative variables \bar{q}_i , for every mesh element i . The flux balance of every element is then approximated as the sum of the interface fluxes to each of the j neighbouring cell:

$$V_i \frac{\partial \bar{q}_i}{\partial t} + \sum_{j \cap i \neq \emptyset} \int_{f_{ij}} \widehat{\mathbf{f} \cdot \mathbf{n}} dS \quad (2.11)$$

where $\widehat{\mathbf{f} \cdot \mathbf{n}}$ is the approximation of the numerical fluxes through the faces. Its computation depends on two elements: the *reconstruction* and the *flux function*. The first defines how the solution at the faces is extrapolated from the cell average \bar{q}_i , using the neighborhood average cell values \bar{q}_j . The second specifies the flux estimation through the boundary from the two reconstructed state vectors on either side of the face. An important observation is that the reconstruction step determines the order of accuracy of the Finite Volume discretization. We can now see the Discontinuous Galerkin Methods as an alternative way to increase the order of the method. Instead of reconstructing the solution at the desired accuracy order from the cells averages, DGM increases the polynomial order in the elements. Following this philosophy, it can be proven that the DG flux function γ_f of a hyperbolic problem can be defined as follow:

$$\gamma_f(u^+, u^-; v^+, v^-; \mathbf{n}) = \llbracket v \rrbracket \cdot \mathbf{n} \mathcal{H}(u^+, u^-, \mathbf{n}) \quad (2.12)$$

where $\mathcal{H}(u^+, u^-, \mathbf{n})$ is the Finite Volume flux function. Defined in this way, DGM inherits the consistency and stability of FVM resulting from the choice of the interface flux \mathcal{H} .

Even if historically Discontinuous Galerkin Methods dealt with hyperbolic problems only, several discontinuous finite element formulations were developed for elliptic problems. These methods are also now considered DGM. One can distinguish two classes of methods: the *Interior Penalty Methods* (IPM) and the *Lifting Methods*. The first can be seen as a generalization of classical continuous finite element methods. The interface fluxes here are defined using a generalization of the boundary penalty methods. An additional penalty term (marked in green), penalizing the difference between the desired solution and the current one, is added to the variational formulation for each element separately to impose continuity of the solution u across the domain:

$$\begin{aligned} \sum_f \int_f \gamma_d(u^+, u^-; v^+, v^-; \mathbf{n}) dS &= \sum_f \sigma_f \int_f \llbracket v \rrbracket \cdot \llbracket u \rrbracket dS \\ &+ \sum_f \int_f \llbracket v \rrbracket \cdot \{\{\mathcal{D} \cdot \nabla u\}\} dS \\ &+ \sum_f \theta \int_f \llbracket u \rrbracket \{\{\mathcal{D} \cdot \nabla v\}\} dS \end{aligned} \quad (2.13)$$

where σ_f is to be chosen such that the positive contribution of the penalty term dominates the boundary flux term (in red), retained for consistency. Therefore to maintain coercivity, σ_f has to be larger than a locally defined critical value σ_c . The blue term is added in variation of the classical formulation, if $\theta = 1$ we obtain a symmetric boundary penalty method (the symmetry of the bilinear form $a(u, v)$ is lost in the classical formulation where $\theta = 0$). If $\theta = -1$, the boundary flux no longer impacts coercivity, and σ_f , in theory, does not have a critical value (it should only be greater than zero). The underlying principles and stability analyses of the *Interior Penalty Methods* are quite close to the standard FEM. The *Lifting Methods* use an auxiliary variational problem to obtain an estimate of the solution gradient, which is then used in a second step to discretize the elliptic equations.

2.1.3. Reynolds Average Navier-Stokes equations

RANS formulation decreases the computational cost of the simulation by introducing statistical models to compute the statistical solution average directly. The user can solve the modeled equations on a coarser grid than the one used for DNS or LES computations, significantly reducing the processing time. However, the statistical character of the solution implies that all the frequencies of the turbulence energy spectrum are modeled, which prevents a fine description of the turbulence physical mechanisms.

The modeled equations are derived from the conservative form of the Navier-Stokes equations through a Reynolds decomposition and averaging. The velocity vector is expressed as the sum of two contributions: the mean velocity \mathbf{U} field and an instantaneous fluctuation \mathbf{u}' field:

$$\mathbf{u} = \mathbf{U} + \mathbf{u}'. \quad (2.14)$$

Then the governing equations are rewritten through an averaging operation (usually an average ensemble [29]). Considering an incompressible flow as an example, one would have:

$$\nabla \cdot \mathbf{U} = 0 \quad (2.15)$$

$$\frac{\bar{D}U_j}{\bar{D}t} = \nu \nabla^2 U_j - \frac{\partial \langle u'_j u'_i \rangle}{\partial x_i} - \frac{1}{\rho} \frac{\partial \langle p \rangle}{\partial x_j} \quad (2.16)$$

where ρ is the flow density, ν the viscosity, p the pressure, $\langle \cdot \rangle$ express the averaging operation, and $\bar{D}(\cdot)/\bar{D}t$ is the mean substantial derivative, which expresses the rate of change following a point moving with the local mean velocity \mathbf{U} :

$$\frac{\bar{D}(\cdot)}{\bar{D}t} = \frac{\partial(\cdot)}{\partial t} + \mathbf{U} \cdot \nabla(\cdot). \quad (2.17)$$

A consequence of the continuity equation (Eq.2.15) is that $\nabla \cdot \mathbf{u}' = 0$. Therefore both \mathbf{U} and \mathbf{u}' are solenoidal fields.

For a general three-dimensional flow, Eq.2.15 and 2.16 are a set of four independent equations governing the mean velocity field. However, these equations contain more than four unknowns. The velocity covariances $\langle u'_i u'_j \rangle$ of Eq.2.16 are un-closed terms, which appear from the averaging operation of the Navier-Stokes equations due to the non-linear convection term. These new unknowns take the name of Reynolds stresses. Making an analogy with the viscous stresses, they can be interpreted as apparent stresses arising from momentum transfer by the fluctuating velocity field. They also characterize the different behavior of the instantaneous velocity field \mathbf{u} to its average \mathbf{U} . Before analyzing the Reynolds stress models proposed to close the equations, we briefly review the properties of $\langle u'_i u'_j \rangle$.

The Reynolds stresses are the components of a second-order tensor, which is symmetric positive semi-definite. Its diagonal components $\langle u'_i u'_i \rangle$ are *normal stresses*, while the off-diagonal components are *shear stresses*. The distinction between these two terms is dependent on the coordinate system choice. An intrinsic tensor decomposition can be made using isotropic and anisotropic stresses. By defining the isotropic component as $\frac{2}{3}k\delta_{ij}$, the deviatoric part is defined as follows:

$$r_{ij} = \langle u'_i u'_j \rangle - \frac{2}{3}k\delta_{ij} \quad (2.18)$$

where δ_{ij} is the Kronecker delta, and k is the *turbulent kinetic energy*, defined to be half the trace of the Reynold stress tensor $k = 1/2 \langle u'_i u'_i \rangle$. An important point in this decomposition is that only the anisotropic component a_{ij} effectively transports momentum.

$$\langle u'_i u'_j \rangle = a_{ij} + \frac{2}{3}k\delta_{ij}. \quad (2.19)$$

Eq.2.15 and 2.16 can be closed by introducing a model that relates the Reynolds stress tensor to averaged quantities. The main closure, used in most of the RANS methods in industrial and academic CFD solvers, is the *turbulent-viscosity hypothesis*, or *Boussinesq's hypothesis*, after Joseph Boussinesq. He proposed it in 1872 during the French Academy of Sciences meeting (the interested reader can find the meeting report in [3]). According to this hypothesis, the deviatoric Reynold stress \mathbf{R} is proportional to the mean rate of strain of the fluid \mathbf{S} (symmetric part of the mean velocity gradient tensor) through a scalar quantity ν_T , called *turbulent viscosity*:

$$\langle u'_i u'_j \rangle - \frac{2}{3}k\delta_{ij} = -\nu_T \left(\frac{\partial U_i}{\partial x_j} + \frac{\partial U_j}{\partial x_i} \right) \quad (2.20)$$

where $s_{ij} = \frac{1}{2} \left(\frac{\partial U_i}{\partial x_j} + \frac{\partial U_j}{\partial x_i} \right)$. Eq.2.20 allows to reduce the number of unknowns in Eq.2.15 and 2.16, the 9 unknown components of the Reynolds stresses are replaced by one scalar unknown $\nu_T(\mathbf{x}, t)$. The closure is finally obtained with an additional transport equation for the evolution of turbulence quantities. As example, two-equation models (such as $k - \varepsilon$ [6] and $k - \omega$ [51]) express the turbulent viscosity as a combination of two turbulent quantities (k and ε or the specific dissipation rate ω) for which additional transport equations are defined. Empirically defined model constants allow for tuning the models for different cases. Instead, one equation models (such as Spalart-Allmaras (SA) [41]) provides an equation for the evolution of one quantity, in the case of the SA model, $\tilde{n}u$, which is then linked to the effective viscosity $\nu_{eff}(\mathbf{x}, t) = \nu + \nu_T(\mathbf{x}, t)$ with a non linear functional relationship. These models are called Linear Eddy Viscosity Models (LEVM), due to the linear relation imposed by Eq.2.20.

A major advantage of the turbulent-viscosity hypothesis is that by replacing Eq.2.20 in Eq.2.16 one obtains the Reynolds equations in the same form as the Navier Stokes equations:

$$\frac{\bar{D}U_j}{Dt} = \frac{\partial}{\partial x_j} \left[\nu_{eff} \left(\frac{\partial U_i}{\partial x_j} + \frac{\partial U_j}{\partial x_i} \right) \right] - \frac{1}{\rho} \frac{\partial}{\partial x_j} \left(\langle p \rangle + \frac{2}{3}\rho k \right) \quad (2.21)$$

where ν_{eff} is the effective viscosity, and $\langle p \rangle + 2/3\rho k$ is the modified mean pressure field. Although it provides a convenient closure to the Reynolds equations, the accuracy of Boussinesq's hypothesis is poor for many flows.

The turbulent-viscosity hypothesis can be divided in two parts: an *intrinsic* assumption and a *specific* assumption [31]. The first implies that at each point and time, the Reynolds stress anisotropy

components r_{ij} are determined by the mean velocity gradients $\partial U_i / \partial x_j$. Therefore, the *local* mean velocity gradients characterize the history of mean distortion to which the turbulence has been subjected, assuming the non-local transport process small in comparison. However, in many flows persisting anisotropies can be found in regions where the local mean strain rate components are zeros. These anisotropies exist because of the prior straining history to which the turbulence has been subjected, and the non-local transport process is not negligible in these cases. The specific assumption is that the Reynolds stress anisotropy tensor r_{ij} is linearly related to the mean rate of strain tensor s_{ij} via the scalar quantity ν_T . This hypothesis is violated even for simple flows (such as shear flows). However, the failure of the linear assumption for many flows of engineering interest (such as boundary layers, shear flows, and jets) does not have important consequences for the final mean flow solution. Yet even for these flows, the predictions of second order moments (Reynolds stresses, kinetic energy, dissipation) are not satisfactory. Moreover, in many configurations of engineering relevance (complex flows having high mixing rates, recirculation regions, stagnation lines) the predictions of these models can be wrong even for first moments.

To overcome the isotropic viscosity hypothesis limitations, corrections were developed for the existing LEVM models, such as the SA-RC [36] and SST-RC [40] models which attempt to account for rotation and curvature effects. An alternative is provide by Non-Linear Eddie Viscosity Models (NLEVM), such as [27, 42]. Another example is given by invariant theory, since the work of Pope [30], it is recognized that it can be used in the framework of turbulence modeling to improve the effective-viscosity hypothesis. In this schemes, the Reynolds stress tensor anisotropic component is developed into a tensor polynomial composed of no more than ten basis tensors:

$$\mathbf{R} = \sum_{i=1}^{10} \lambda_i \mathbf{T}_i \quad (2.22)$$

where a_i are flow scalar invariants and the tensorial basis \mathbf{T}_i can be expressed as products of the mean strain tensor \mathbf{S} and the mean vorticity tensor \mathbf{W} . The advantage of these formulations is that the whole velocity-gradient tensor now affects the predicted Reynolds stresses, as a consequence the influence of the streamline curvature on \mathbf{R} is embedded in the model. However, the model still implies the intrinsic assumption. Its accuracy is therefore limited to flows where the non-local transport process can be neglected. Non-local models that take into account the prior straining history of turbulence have been proposed to overcome this limitation, for example, the Lag-RST model [28].

3

Flow Description and Computational Setup

This work studies a three-dimensional turbulent flow over a NACA-0012 half wing mounted at the wall, with a rounded end cap and trailing edge. Two flow conditions were investigated: $Re = 4.3 \times 10^6$ and $Re = 1.2 \times 10^6$. The Reynolds number refers to the free stream conditions, and it was defined as $Re = U_\infty c / \nu$, where U_∞ is the unperturbed free stream velocity, c the chord length, and ν the kinematic viscosity. The flow is characterized by a high three-dimensional flow caused by the pressure difference that is established between the pressure and suction side of the wing. The latter generates flow whipping around the tip, and the surface streamlines deviate outboard on the pressure side and inboard on the suction side.

At the wing cap, the flow separates and roll-up into a vortex, fed by the boundary layer vorticity close to the tip. As the vortex moves downstream, it rolls up more and more of the wing wake until its circulation is nominally equal to that of the wing. Grow [16] reports that 90% of the circulation enters the tip vortex within one chord of the trailing edge. Several authors report the presence of secondary and tertiary vortices, which, as they become wrapped up into the primary vortex, cause a rapid change of direction of the vortex core [7, 46, 13, 15]. This behavior is reported in the literature as "vortex kink". The vortex centerline undergoes a sudden spanwise cross-flow acceleration at the beginning of the kink, and at its end, it resumes its original direction. The wing cap shape is reported to influence the vortices location and the number of vortices forming [46]. Guini [13, 15] and Guini & Benard [14] report that a 'more' axisymmetric vortex sheds from a rounded wingtip with stronger vorticity within its core compared to a square-tip wing.

RANS simulations were conducted using the finite volume open source software SU2 to study the flow. Furthermore, implicit LES computations were carried out on 10% of the wing span using the Discontinuous Galerkin software ARGO. The latter was considered to be located far from the wingtip, and from the wind tunnel wall where the wing is mounted, so periodic boundary conditions could be used.

3.1. Computational domain

The rectangular half-wing numerically investigated has a NACA-0012 profile, with a rounded wing cap and trailing edge. Its aspect ratio is $AR = 0.75$, and it is mounted midway up a wall at its quarter chord, pitched up by 10° .

The computational domain, shown in Fig.3.1, is based on the test section of the low-speed wind tunnel used by Chow, located in the Fluid Mechanics Laboratory of NASA Ames Research Center. The numerical test case exactly represents the experimental cross-section $0.66c \times 1c$, where c is the airfoil chord. At the same time, it uses a greater stream-wise domain extent L to assure that the computed solution is free of boundary effects. L was selected such that the domain mimic Churchfield's one for the RANS computations and that of Lombard for the LES simulations.

The reference frame used in the simulations is a Cartesian coordinate system (x, y, z) . Its origin is located at the wing trailing edge. The x axis is aligned with the stream-wise direction, the z axis is

Test case	L	l_1	l_2
Chow et al.	$1.813 c$	$0.396 c$	$1.417 c$
Churchfield et al.	$5.5 c$	$2.5 c$	$3 c$
Lombard et al.	$10 c$	$3 c$	$7 c$
RANS SU2	$5.5 c$	$2.5 c$	$3 c$
LES ARGO	$10 c$	$3 c$	$7 c$

Table 3.1: Stream-wise domain extent L for different test cases. The values l_1 and l_2 correspond to the distance of the wing quarter cord to the inflow and outflow boundary, respectively.

directed towards the wing tip, and y is directed orthogonal to form a right-handed coordinate system, as shown in Fig.3.1.

In his paper, Chow warns against significant inviscid effects (mirror effects) linked to the proximity of the walls, which most likely influence both the primary and secondary vortices. Lombard also noted that the significant blockage created by the wing is likely to cause an absolute perceived angle of attack around 2° higher than the one imposed by the geometry. The numerical simulations do not reproduce the boundary layer tripping mechanism used in the experimental setup of Chow. Moreover, the wind tunnel sections upstream and downstream of the test section and the influence of the probes presence are not modeled. McAlister and Takahashi [24] report that the tripping of the boundary layer near the leading edge increases the vortex's diameter by 30%. Moreover, it decreases the inboard movement of the primary vortex along the span.

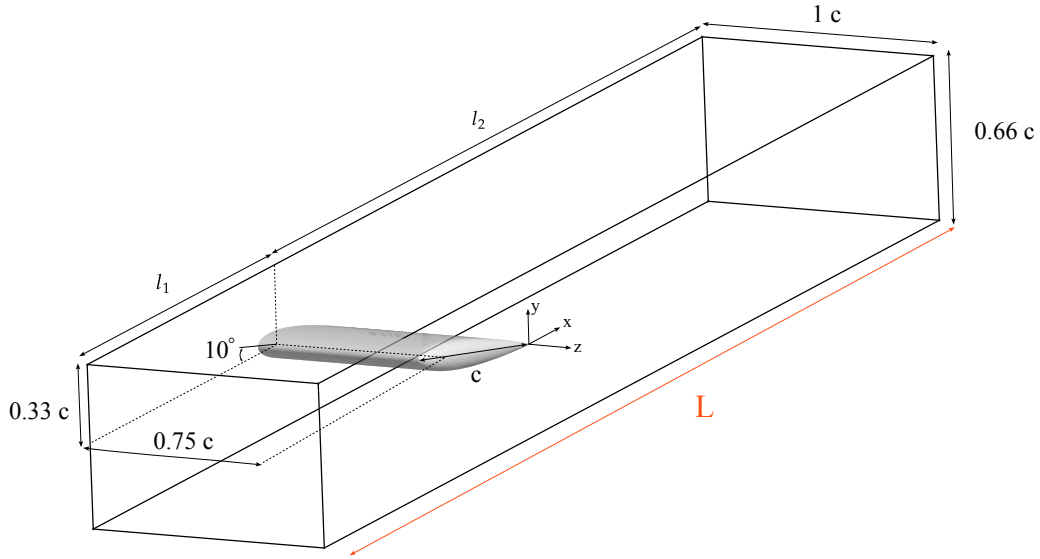


Figure 3.1: Simulations computational domain. The flow is aligned with the x -axis. The lengths l_1 and l_2 are the distance of the wing quarter cord to the inflow and outflow boundary, respectively. The lengths L , l_1 and l_2 changes in relation to the test case considered (see Tab.3.1).

Test case	Inflow turbulence	Tunnel walls	Outflow
Chow et al.	$I < 15\%$	no slip	-
Churchfield et al.	$I = 0.1\%$	no slip	Constant mass flow rate
Lombard et al.	Not modeled	free slip	Dong et al. outflow BC [11]
RANS SU2	$I = 0.1\%$	free slip	Characteristics-based Riemann BC [49]
LES ARGO	Not modeled	free slip	Mesh coarsening

Table 3.2: Principal boundary conditions differences for the numerical and experimental setups. $I = u'/U$ is the turbulence intensity, where u' is the root-mean-square of the turbulent velocity fluctuations and U is the mean flow velocity.

3.2. Boundary conditions

Tab. 3.2 reports the principal differences in the boundary conditions (BC) used by each setup. Special attention is given to the outflow boundary condition choice due to the presence of the low-pressure vortex core. Indeed if a constant pressure outflow boundary is used, the vortex, generated at the wingtip and convected downstream out of the domain, would encounter large pressure gradients. It should also be noted that only the numerical simulation of Churchfield et al. models the wind tunnel boundary layer. The choice of using free slip boundary conditions in the other computation is justified by the primary vortex location, which is sufficiently far from the walls so that the interaction with the latter is much weaker than the one with the wing surface via the secondary structures. The inviscid interaction between the vortex and the wind tunnel wall is assumed to be similar to the experimental one. The specific boundary and initial conditions used for the numerical simulations are reported in the following sections.

3.2.1. RANS boundary conditions

For the test case run at $Re = 4.3 \times 10^6$, the free stream conditions were chosen in order to match those of Chow's experiment: $Re = 4.6 \times 10^6$ and $M = 0.15$. One should notice that Chow's reference location, $x = -1.1344c$, $y = 0.3423c$ and $z = 0.0969$, is just upstream of the suction side of the wing. Here the flow has accelerated more than the one at the inflow location. Hence a lower free stream computational Reynolds and Mach number should be used to match the same conditions. Consequently they are set to $Re = 4.3 \times 10^6$ and $M = 0.14$. The free stream Prandtl number is $Pr = \nu/\alpha = 0.72$, where α is the thermal diffusivity. An adiabatic, viscous wall condition is imposed at the wing surface, while a free slip condition is used for the tunnel walls.

A characteristics-based Riemann boundary condition proposed by Vitale et al. [49] is imposed at the outflow. This boundary condition automatically detects inflow/outflow boundaries for hyperbolic systems, following the approach proposed by Guardone, Isola and Quaranta [17]. Then using an eigenvalue analysis, the right number of enforceable unknowns is determined, and the variables that can be specified at the boundary are automatically selected. Only the variables transported from the boundaries towards the interior are enforced, while the remaining variables are extrapolated from the internal solution. On the SU2 suite, the Riemann boundary marker requires setting the total temperature and pressure at the inflow and the static pressure at the outflow. They were chosen to obtain the desired free stream Mach number. The total conditions are $P_0 = 170891$ Pa and $T_0 = 298$ K, while the static pressure is $P = 168399$ Pa.

The lower Reynolds simulation uses the same boundary conditions of the previous case, only changing the free stream conditions to match those of Lombard, while preserving the same mass flow of the Chow experiment. The Reynolds and Mach numbers are $Re = 1.2 \times 10^6$ and $M = 0.1$.

3.2.2. LES boundary and initial conditions

The LES boundary conditions were set to match the Reynolds and Mach number used by Lombard, $Re = 1.2 \times 10^6$ and $M = 0.1$. The free stream Prandtl number is $Pr = 0.72$. At the inflow total conditions are imposed, $P_0 = 101325$ Pa and $T_0 = 288.15$ K, while at the outflow we impose a static pressure, $P = 100277$ Pa. To avoid large pressure gradients at the outflow, a longer stream-wise domain extent

is used, combined with a coarser mesh toward the outlet. Since ARGO is an implicit method, coarsening the mesh is equal to adding dissipation at that location, as seen in Sec.2.1.1. Therefore the vortex is disrupted before arriving at the outflow boundary. An adiabatic viscous wall condition is imposed at the wing surface, while a free slip condition is used for the tunnel walls.

The flow is impulsively started from $U_\infty = 17$ m/s throughout the domain, except at the no-slip boundaries. Then it gradually increase to $U_\infty = 34$ m/s. The initial pressure and temperature are $P = 101325$ Pa and $T = 288.15$ K.

3.3. Numerical schemes

3.3.1. SU2 solver

The SU2 RANS compressible solver was used for the LEVM computations. Two turbulence models were investigated, the Negative Spalart-Allmaras and the Menter's Shear Stress Transport model. The first is a variation of the standard one equation model developed to address issues with under-resolved grids and non-physical transient states. It is recommended because it is formulated to be passive to the original SA model in a well-resolved flow field but has a more robust numerical behavior. The SST model instead is a two-equation model that combines $k - \omega$ and $K - \epsilon$, using the first in the inner region of the boundary layer and switching to the second in the free shear flow.

The following set-up was used for both turbulence models and Reynolds numbers investigated. The implementation parameters are reported in Tab.3.3. The free-stream values, defined in Sec.3.2.1, are not only used as boundary conditions but also for flow initialization and non-dimensionalization. The flow physical definition is based on the free-stream description, combined with an ideal gas and constant viscosity assumptions.

The convective fluxes through the faces of the dual-grid control volumes are discretized using a central scheme: the Jameson-Schmidt-Turkel (JST) method with matrix dissipation. In this approach, the classical JST implementation's second and fourth-order dissipation coefficients (β and η) are scaled by the flux Jacobian with the minimum eigenvalue limited by the entropy fix coefficient ψ . We chose this alternative formulation because it gives better viscous drag predictions on low-Re meshes than the classic one. Tab.3.3 reports the list of parameters used in the computation.

Even if we perform a steady computation, we need to define a time discretization scheme since the solver uses a pseudo-time iteration. Therefore, we used an Euler implicit approach. The option "central jacobian fix factor" a is also used to improve the numerical properties of the Jacobian matrix in the implicit time marching formulation so that higher Courant–Friedrichs–Lewy (CFL) values can be used. CFL adaptation is employed to accelerate convergence to a steady state. Within this procedure, the CFL is initialized at a value CFL_0 , then its value at each iteration is determined based on the residual value at the current e_{new} and previous e_{old} iterations, as $CFL = CFL \cdot (e_{new} - e_{old})^b$. The value of b is chosen depending on whether e_{new} is greater or lower than e_{old} , increasing it by factor up or decreasing it by factor down.

3.3.2. ARGO solver

The flow properties were modeled in the LES computation using an ideal gas and a constant viscosity assumption. The initial pressure and temperature defined in Sec.3.2.2 were used to non-dimensionalize the unsteady Navier-Stokes equations. The convective flux (Eq.2.10), coming from the Discontinuous Galerkin formulation, is defined using a Simple Low Dissipation Advection Upstream Splitting method (SLAU), which essentially solves a Riemann problem at the elements' interfaces. The diffusive terms (Eq.2.13) are instead discretized using a Symmetric Interior Penalty method for Discontinuous Galerkin (SIPDG). We use the nodal shape function defined by third-order Lagrange interpolants to discretize the solution. The control points used are equispaced. The simulation parameters are reported in Tab.3.4.

The solution's temporal evolution is discretized using a backward difference formula: BDF2. To save computational resources, we only compute the Jacobian matrix every five time steps, freezing it for the others. The choice of the time step Δt was dictated by stability and computational cost requirements. The value used in the computation corresponds to a through-flow time every 10^4 iterations, where the through-flow time $\Delta t_{TF} = c/U_\infty$ is defined as the time required by a flow particle to cross the wing chord.

The non-linear system of partial differential equations is then solved using a Newton-GMRES approach with a line implicit preconditioner, where GMRES stands for generalized minimal residual method.

Parameter	Value
β	0.5
η	0.02
ψ	0.01
a	8.0
factor up	2.0
factor down	0.1
CFL ₀	2.5

Table 3.3: List of parameters used in the SU2 solver.

Parameter	Value
$\max(n_{NL})$	5
Non-linear tolerance	10^{-4}
$\max(n_L)$	30
GMRES tolerance	10^{-2}
Krylov subspace size	30
Δt	$3 \times 10^{-6} \text{ s}$
Δt_{TF}	$2.9 \times 10^{-2} \text{ s}$

Table 3.4: List of parameters used in the ARGO solver. Where $\max(n_{NL})$ is the maximum number of iterations of the non-linear solver required to reach the tolerance within a time step. While $\max(n_L)$ is the maximum number of iterations of the GMRES scheme to reach convergence.

In the latter, the solution of the linear system generated by one step of the Newton algorithm is approximated by the vector in a Krylov subspace with minimal residual. As done for the time marching scheme, the Jacobian matrix, coming from the Newton scheme, is only computed every five steps to save computational resources. The integrals computed within each element are approximated with a seventh-order Gauss-Legendre quadrature rule. The quadrature order is increased to eleven in regions with high gradients.

3.4. Mesh generation

3.4.1. RANS mesh

The numerical grid used to compute the RANS simulations is a linear straight-sided grid created with the commercial mesh generator ANSYS ICEM. This software provides a robust and intuitive approach, which offers high control on the definition of the elements. The mesh was used for both turbulence models and Reynolds numbers investigated.

In ICEM, the grid generation is based on the domain division in "blocks". Two blocks were placed around the wing to have more control over the wingtip mesh, one that encloses the wing cap and the other in the remaining part. During the mesh convergence study, it was observed that a higher grid density is required in the wing tip and the region close to it on the wing suction side to catch the physics of the vortex forming there correctly. Therefore the span-wise element spacing is reduced from 0.01 at the root to 0.0035 where the wing tip starts its revolution. The wing tip grid spacing is 0.005. To model their curvature correctly, the element spacing is also reduced in the stream-wise grid from 0.01 to 0.0025 at the leading and trailing edge regions. The placement of the first grid cells close to the wing surface is such that it satisfies $y^+ < 1$, where $y^+ = u_* n / \nu$, with n the direction normal to the surface, and $u_* = \sqrt{\tau_w} / \rho$ the friction velocity (τ_w is the wall shear stress). When marching grids out from a surface to create a volume, stretching ratios are equal to 1.05 and 1.1. A larger stretching ratio of about 1.5 is used only at the inflow boundary. Tab.3.5 reports the total number of grid points used at the principal mesh locations.

The mesh convergence study is presented in Fig.3.2. The study was conducted on the wing surface, and vortex centerline means quantities will be compared to the literature references in the results, Sec.4. The degrees of freedom of the mesh used in the study are reported in Tab.3.6. The final mesh chosen is "mesh 6".

It should be observed that the mesh used in the present study has 4.03×10^6 degrees of freedom, while the grid used by Churchfield is composed of 70% more: 13.8×10^6 . We observe that the use of viscous tunnel walls boundary conditions in the computations of Churchfield requires satisfying the requirement $y^+ < 1$ at every wall, which implies a higher number of grid points to be used than the case with inviscid boundary conditions. Therefore we observe that despite the significant difference

Location	Grid points number	Mesh	DOF
Stream-wise grid line wake	300	mesh 1	0.79×10^6
Span-wise grid line wake	115	mesh 2	0.95×10^6
Stream-wise grid line wing	120	mesh 3	1.14×10^6
Span-wise grid line wing	65	mesh 4	2.7×10^6
Leading edge	28	mesh 5	3.2×10^6
Trailing edge	28	mesh 6	4.03×10^6
Wing-tip revolution	78	mesh 7	4.7×10^6

Table 3.5: Number of grid points of the final mesh used for the RANS computations ("mesh 6" of Tab.3.6). **Table 3.6:** Grids degrees of freedom used for the convergence study.

in the total number of degrees of freedom of the grid, the refinement of the present study on the wing surface and the vortex location meshes is comparable to that used by Churchfield. We also observe that the refinement and the total number of degrees of freedom used in the present study are similar to the one recommended by other authors to obtain grid-independent behavior [26, 9].

3.4.2. LES mesh

When computing high-order simulations, an accurate representation of the domain geometry is essential to reproduce the physics that forms near the boundaries. To define the numerical grid for the LES computations, we have relied upon the open source mesh generator GMSH, which supports high-order elements. Fig.3.4 presents an overview of the unstructured mesh generated.

The mesh was created by defining a two-dimensional mesh, which was then extruded in the span direction so that periodic boundary conditions could be imposed at the left and right walls. The boundary layer region presents a structured mesh with curved elements describing the wing geometry. A fast curving algorithm was used to optimize the high-order element creation. The first cell spacing to the wing surface is $5e-5$, then the grid spacing is increased with a stretching ratio of 1.1, and the distance between the first and last cell of the "boundary layer mesh" was set to 0.05. The element spacing in the span-wise grid line is 0.004, while the stream-wise direction is 0.005. The spacing is set at the leading and trailing edge to one grid point every 10° . For this surface discretization we have $x+ = 200$ and $y+ = 2.5$ on average, where $x+ = u_* s / \nu$, with s the direction tangential to the surface, and $y+$ defined as explained in the RANS mesh. An overview of the $x+$ and $y+$ distribution over the airfoil can be observed in Fig.3.5. Although we recognize that this value of $x+$ is not optimal, the mesh was not further refined due to computational cost limitations.

The maximum element size in the "boundary layer" mesh and the highly refined grid around the airfoil is 0.01. The mesh is progressively coarsened toward the tunnel walls and, after 1.25 chord lengths going to the outlet. The size of the coarser elements at the inflow and outflow is 0.11. We observe that the mesh was generated without prior knowledge of the flow. After observing the results, it should be noticed that the extension of the highly refined region around the airfoil can be decreased to add more resolution in the tangential airfoil direction and therefore decrease $x+$ without additional computational costs.

The boundary layer mesh is composed of 285984 hexahedra, while the rest of the mesh is formed by 480654 prisms. Running the computations with third-order polynomials, the total degrees of freedom are 37.5 million.

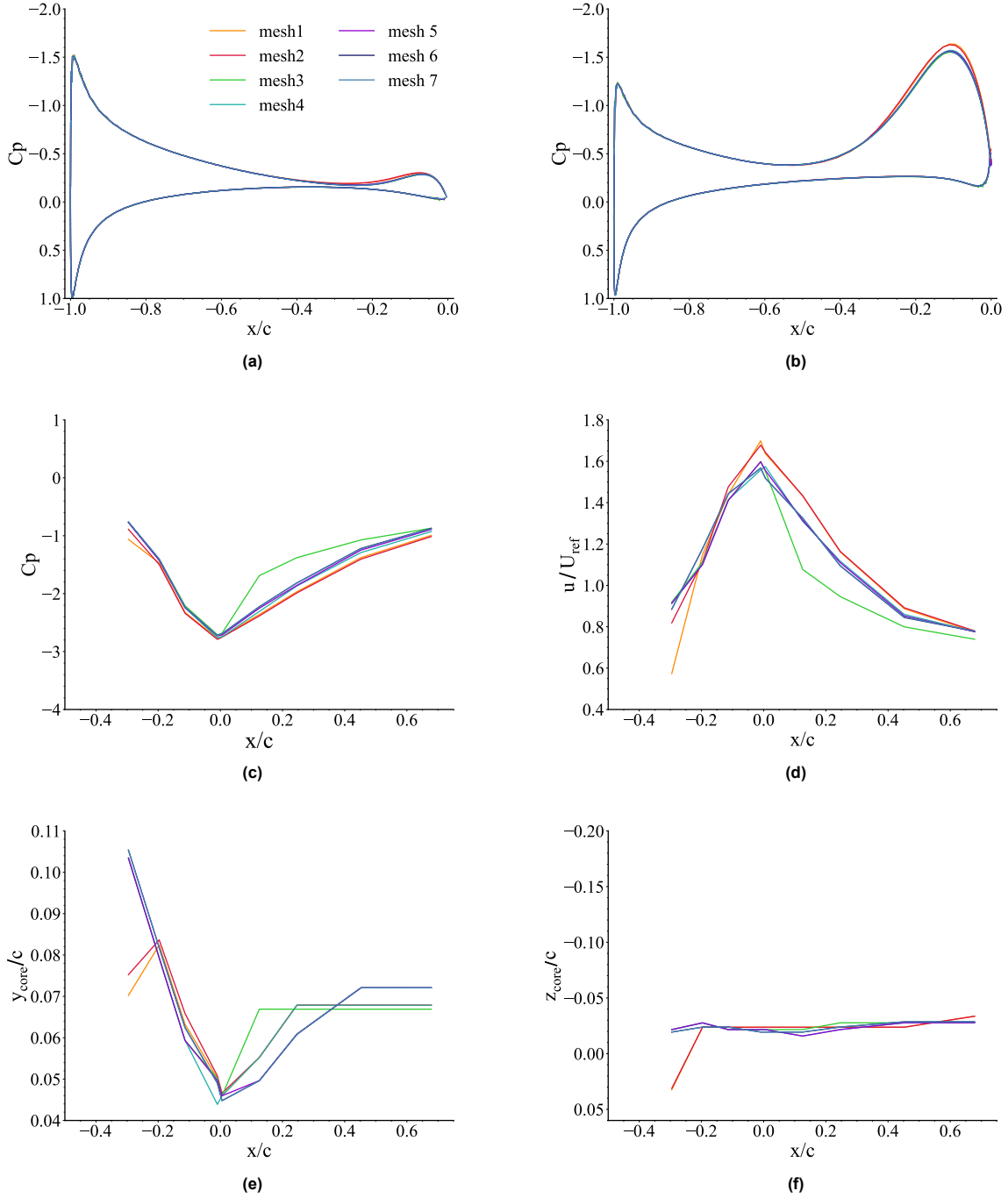
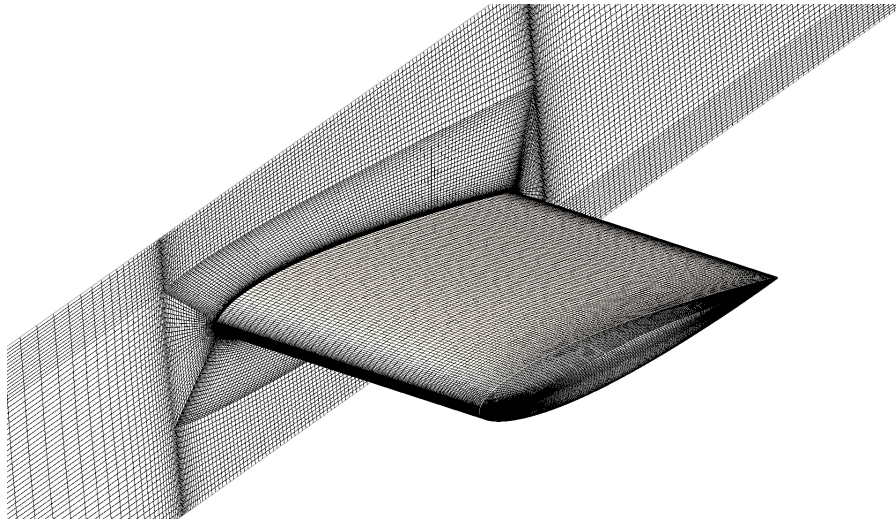
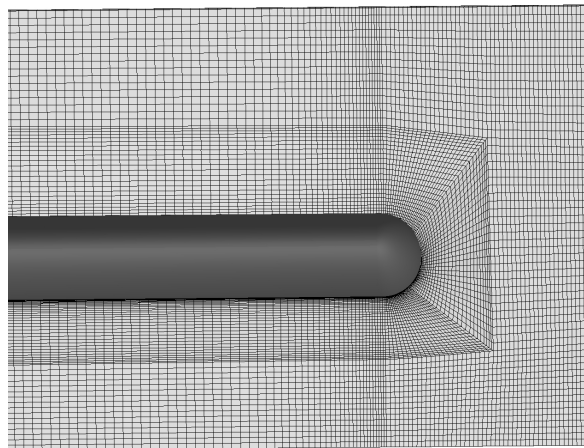


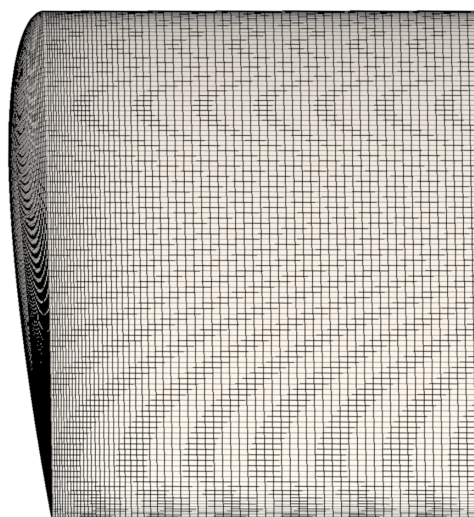
Figure 3.2: Mesh convergence study. (a) Static pressure coefficient distribution along the wing chord at $z/c = -0.065$; (b) Static pressure coefficient distribution along the wing chord at $z/c = -0.023$; (c) Static pressure coefficient evolution along the vortex centerline; (d) Axial velocity evolution along the vortex centerline; (e) Vortex centerline position in the x-y plane; (f) Vortex centerline position on the x-z plane. The static pressure coefficient is defined as $c_p = (P - P_{ref}) / (0.5\rho U_{ref}^2)$. The reference quantities are considered at $x = -1.1344c$, $y = 0.3423c$ and $z = 0.0969$ (same reference location as Chow and Churchfield). The reference frame is shown in Fig.3.1



(a) Wing and left plane mesh.

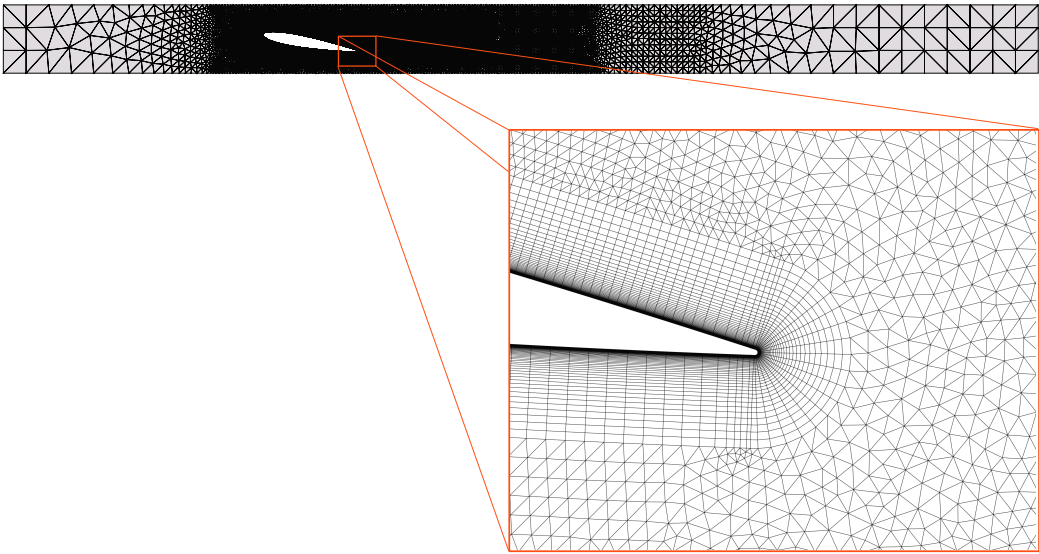


(b) Stream-wise plane cut at the wing mid chord.

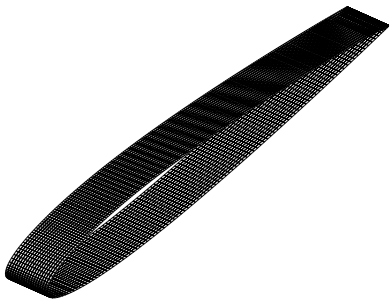


(c) Wing surface mesh.

Figure 3.3: Overview of the mesh generated with ICEM.



(a) Span-wise plane cut.



(b) Wing surface mesh.

Figure 3.4: Overview of the unstructured higher-order mesh generated with GMSH.

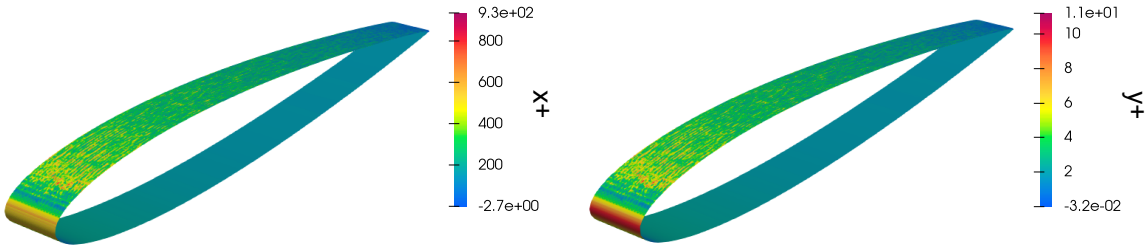


Figure 3.5: Surface distribution of x^+ and y^+ .

4

Results and discussion

4.1. Wing surface

4.1.1. Skin friction field

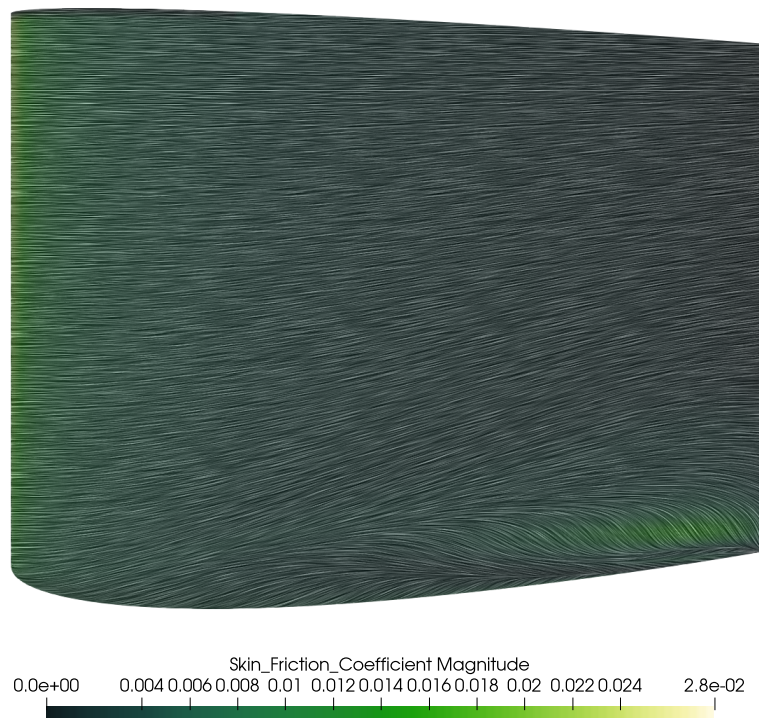
When studying complex three-dimensional flows, the skin friction field visualization allows inferring distinct topological features of the near-wall flow [22]. Fig.4.1 and 4.2 show the wing surface skin friction lines obtained with the SA-NEG turbulence model. No apparent differences are observed in the SST model results. From Fig.4.1 we can observe the highly three-dimensional nature of the flow near the wing cap. Due to the span-wise pressure gradient (Fig.4.7) generated by the wing tip leakage, the flow streamlines deviate outboard on the pressure side and inboard on the suction side. The skin friction lines mirror this behavior. Away from the tip, instead, the skin friction lines are quite two-dimensional.

On the suction side, after about 55% of the chord near the wing cap, there is a region of skin friction lines that are skewed outboard converging to the same line. Fig.4.2 clearly shows two converging lines, one in the wing cap and one in the suction side at the beginning of the wing tip revolution, separated by a diverging line. No singular points are observed in the skin friction line topology. As observed by many authors in numerical simulations and experiments [47, 5, 37, 10], skin friction lines converging to, or diverging from, a line is an on-wall signature of three-dimensional flow separation (line convergence) and reattachment (line divergence).

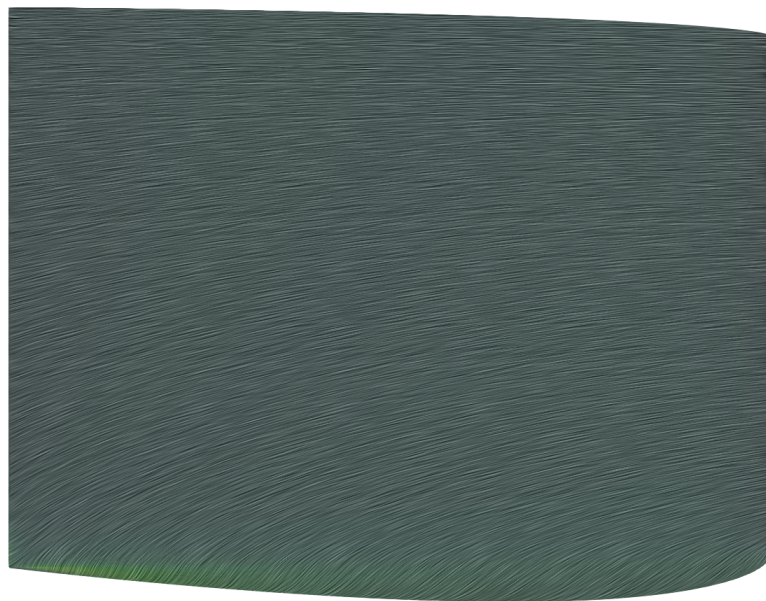
In contrast to what Prandtl [32] showed for a two-dimensional steady flow ¹, the presence of singular points is not a necessary condition for separation in three-dimensional flows. Only the existence of a converging line is required. The separation mechanism of three-dimensional flows along a converging line that does not emanate from a saddle point is reported in the literature as "open" separation [50], by contrast to the "closed" type postulated by Lighthill [19]. It is also called a local separation line because it does not lead to a global separation, characterized by a zone of stagnant fluid or reversed stream-wise flow, but only to the local departure of the shear layer from the surface. By looking at Fig. 4.3, 4.4, and 4.5 we can observe the open separation mechanism. The shear layer departs from the surface at the first converging line in the wing tip and wraps up to feed a vortical structure. The divergent line instead corresponds to a region of flow reattachment. Two vortices can be observed, a primary one above the wing and a secondary smaller vortex placed underneath the first shifted to the left. They can be distinguished by the presence of a saddle point in the cross-flow velocity, which can be better seen in Fig.4.16. Their interactions and influence are hard to infer. As we move from $x/c = -0.2$ (Fig.4.3) to $x/c = -0.125$ (Fig.4.4) we observe that the first vortex size has increased and its core has moved upward. By looking at the velocity on the XY plane (Fig.4.5), we observe that the second converging line is a signature of flow departure from the surface, which moves upward to the primary vortex location.

The surface oil flow visualization of Chow reports a highly similar flow topology. The main difference is observed at the wing root. At this location, the experimental results show skin friction lines slightly moved outboard due to a horseshoe vortex generated by the wing junction with the viscous wall.

¹For two-dimensional flows, Prandtl showed that separation from a no-slip boundary takes place at isolated points where the wall shear stress vanishes.



(a) Suction side



(b) Pressure side

Figure 4.1: Skin friction lines on the wing surface, colored by the skin friction coefficient $c_f = \tau_w / (0.5\rho U_{ref})$. Where τ_w is the wall shear stress. The lines were obtained using the line integral convolution (LIC) vector field visualization in the open source software Paraview.

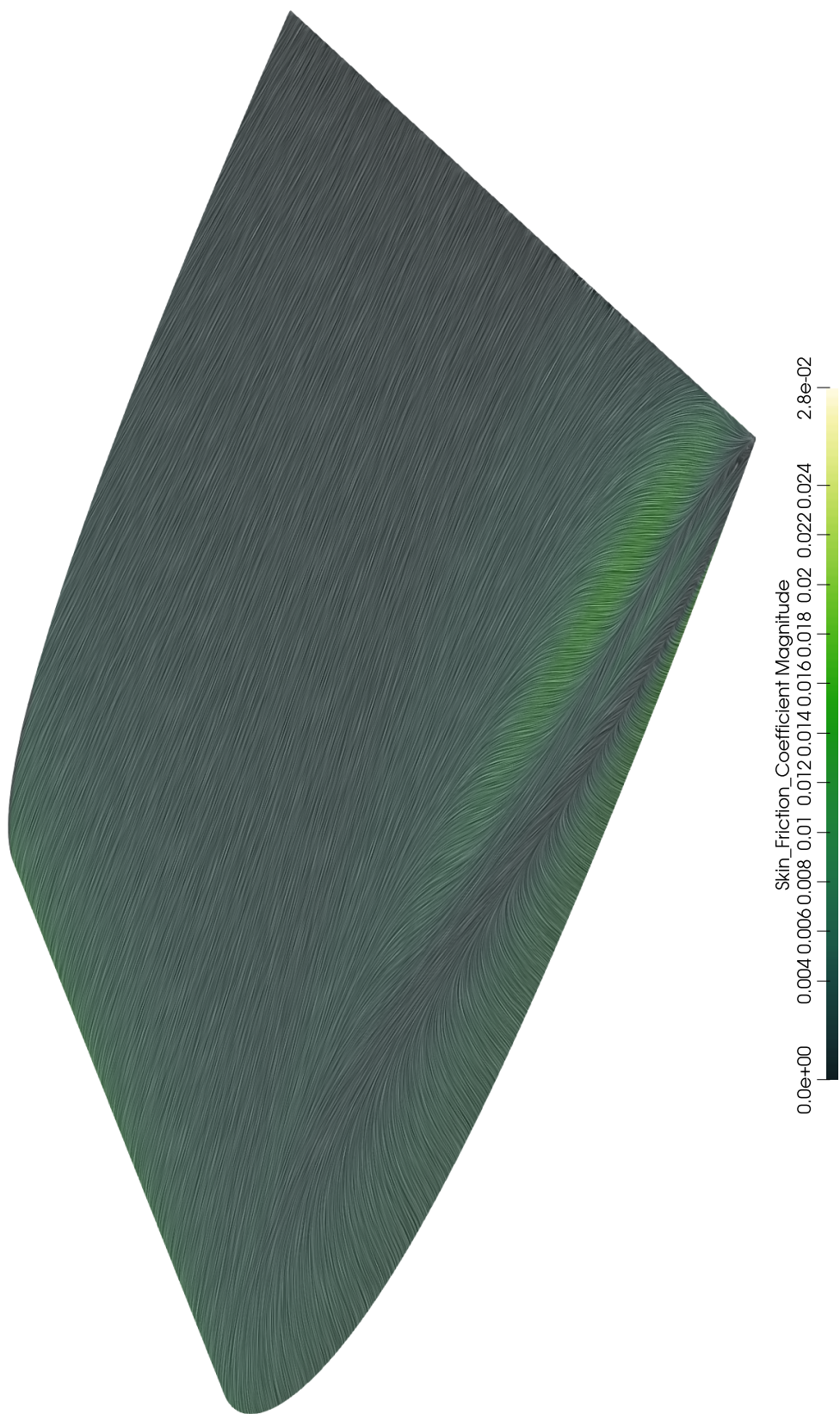


Figure 4.2: Wing tip view of the skin friction lines on the wing surface, colored by the skin friction coefficient c_f . The lines were obtained using LIC vector field visualization in the open source software Paraview.

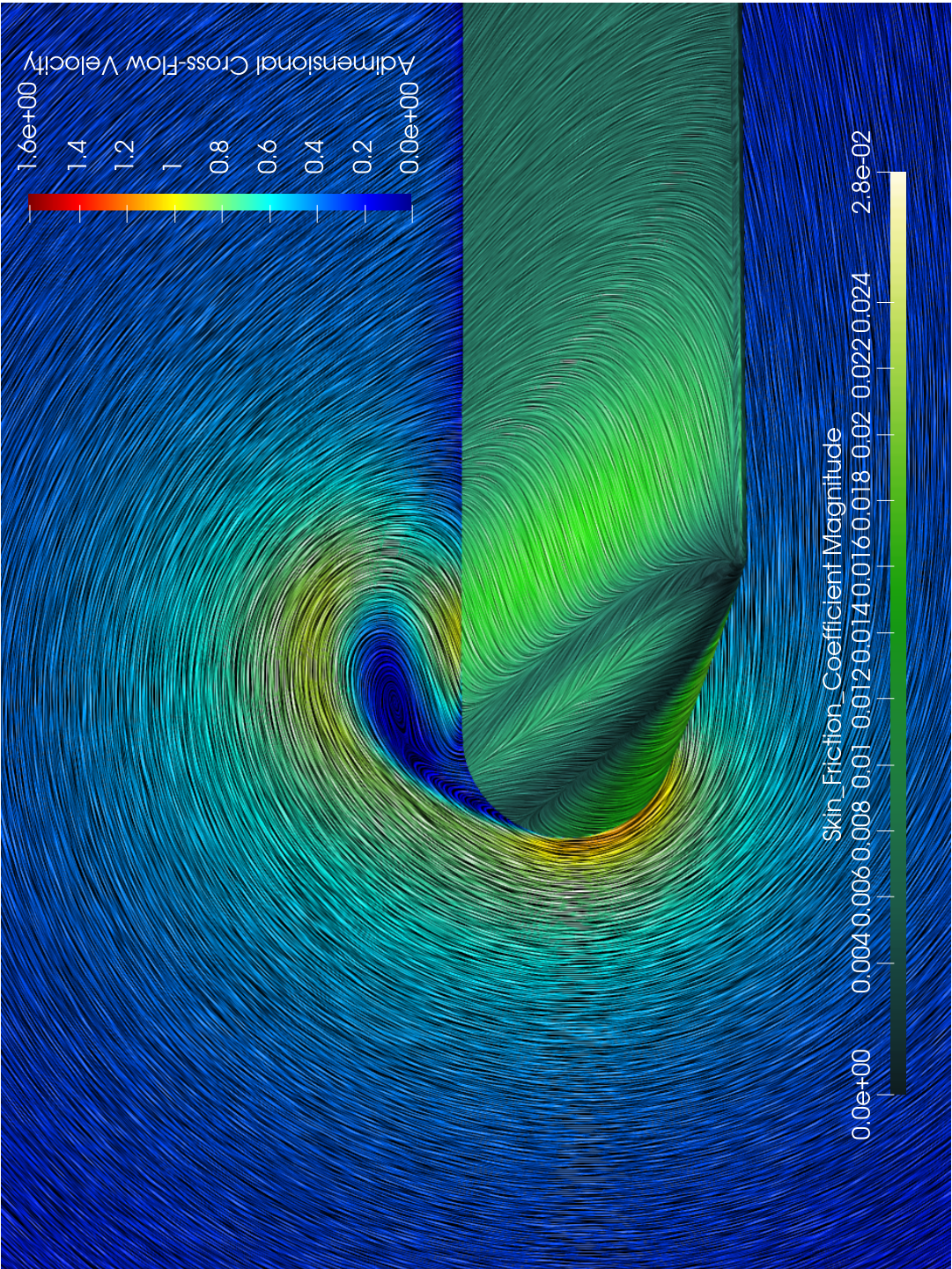


Figure 4.3: Wing surface skin friction lines combined with the xz cutting plane cross-flow lines at $x/c = -0.2$. Both the cross-flow and the skin friction vector field were visualized with LIC vector field visualization in the open source software Paraview. The skin friction lines are colored by the skin friction coefficient c_f , while the cross-flow lines are colored by the adimensional cross-flow velocity U_{cf}/U_{ref} .

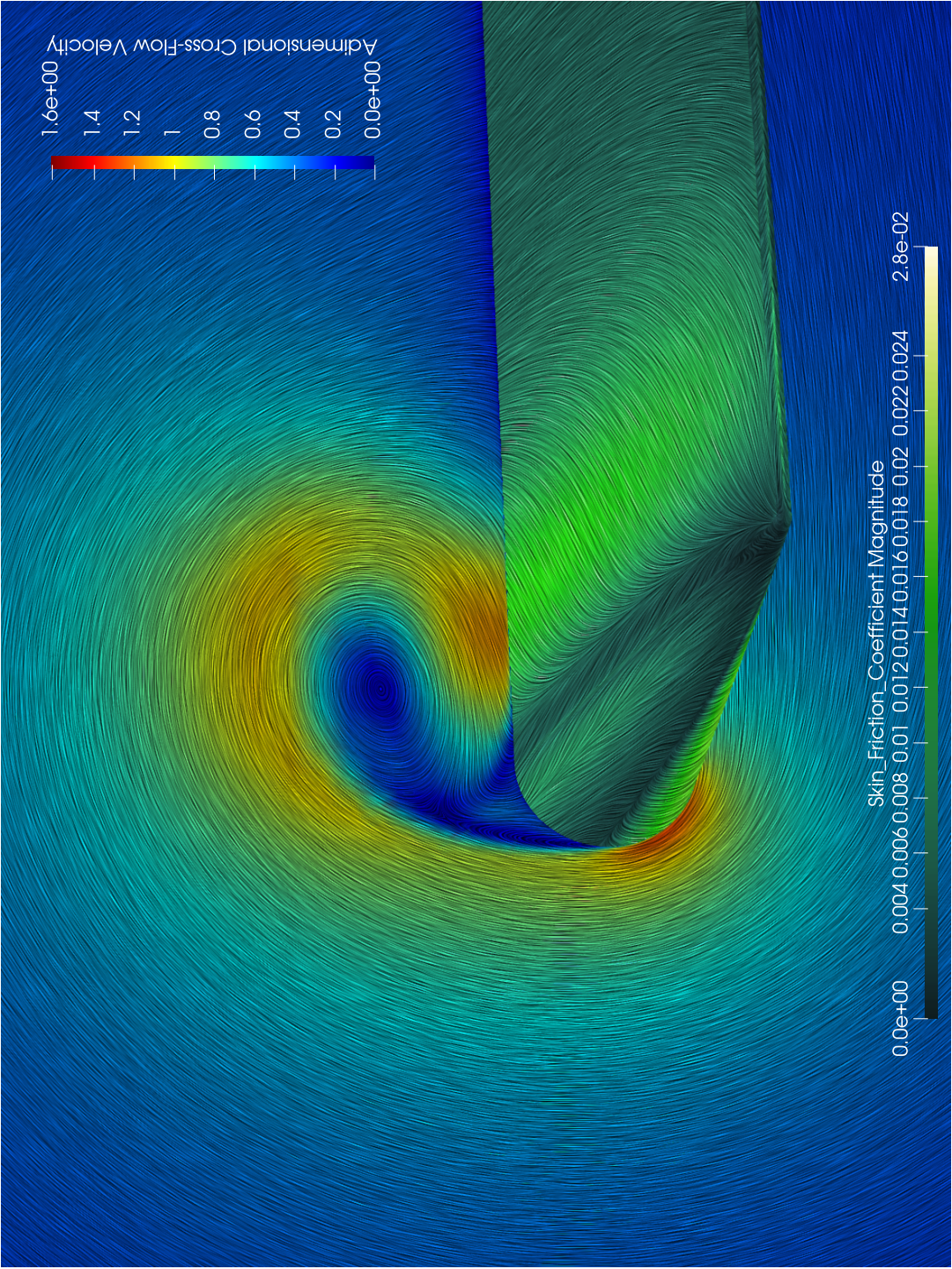


Figure 4.4: Wing surface skin friction lines combined with the xz cutting plane cross-flow lines at $x/c = -0.125$. Both the cross-flow and the skin friction field were visualized with LIC vector field visualization in the open source software Paraview. The skin friction lines are colored by the skin friction coefficient c_f , while the cross-flow lines are colored by the adimensional cross-flow velocity U_{cf}/U_{ref} .

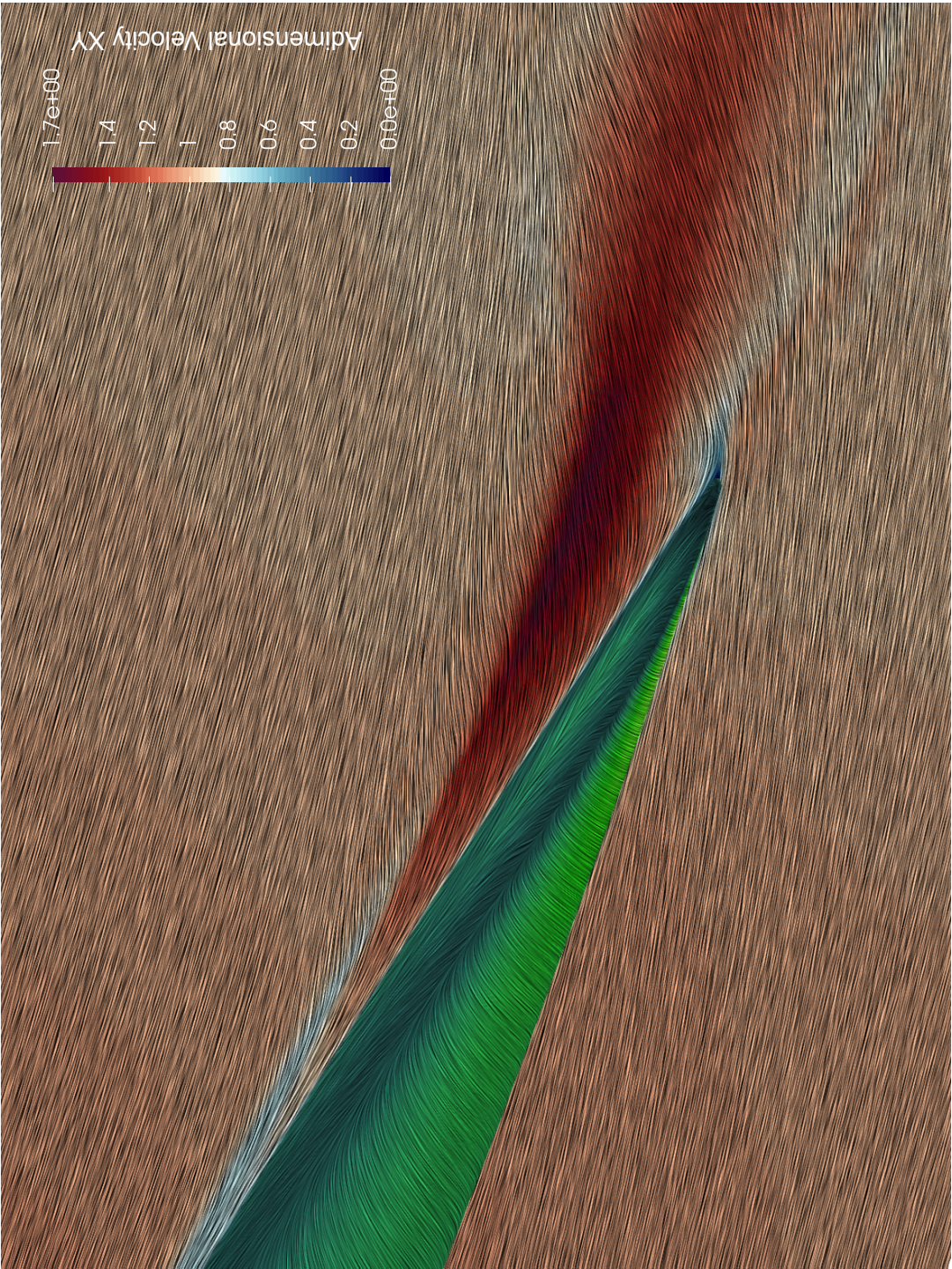


Figure 4.5: Skin friction lines on the wing surface combined with the velocity field projected in the xy cutting plane at $z/c = -0.005$. The skin friction lines are colored by the skin friction coefficient c_f , while the velocity lines are colored by the adimensional velocity projected in the XY plane U_{xy}/U_{ref} . The velocity and skin friction field were visualized with LIC vector field visualization in the open source software Paraview.

4.1.2. Pressure field

The surface pressure results corroborate the flow features inferred from the skin friction field visualization. The span-wise pressure gradient generated by the finite wing that causes the streamlines deviation can be observed in the static pressure coefficient contours in Fig.4.7, where $C_p = (P - P_{ref}) / (0.5 \rho U_{ref}^2)$. The suction side is more excited by the wing tip flow leakage. The stagnation line is nearly straight for most of the span on the pressure side, while it significantly reduces on the suction side near the wing cap region (as can also be observed in Fig.4.10a). The minimum pressure coefficient is $C_{p_min} = -2.9$, which is 9.8% lower than the one reported by Chow. Away from the wing tip, the flow approaches two-dimensional behavior in both the pressure and suction sides. On the latter, we observe a favorable pressure gradient on the x-direction for about 60% of the chord. This result is in good agreement with what was observed by Chow.

Fig.4.8 gives a better view of the static pressure coefficient distribution along the wing cap. In the initial portion of the wing tip, far from the separation lines seen in the skin friction results, the surface pressures taper off to gradually equalize themselves at the wing tip. Instead, on the suction side in the lower rear part of the wing tip, the presence of the primary vortex causes a suction peak, colored in green in Fig.4.8. The vortex and its core can be clearly identified in the streamlines visualization in Fig.4.9. Recalling Fig.4.3 and 4.4, we observe that this suction region is located next to the upper open separation line and corresponds to highly skewed outboard skin friction lines. Given that the primary vortex is rotating in a clockwise direction, we can assume that the vortex is inducing a cross-flow velocity component on the surface that contributes to the surface streamlines deviation. The latter, in turn, causes a tangential velocity and pressure decrease on the surface and, therefore, the suction peak. A larger suction region is observed in the lower rear part of the wing tip next to the tip separation line. Recalling Fig.4.2, we notice that this region corresponds to highly curved skin friction lines caused by flow whipping around the tip. These two suction regions are also observed in the experimental results of Chow.

A significant difference between the SA-NEG (Fig.4.7a) and SST (Fig.4.7c) turbulence models results is the stream-wise extension of the suction region below the primary vortex. The SST model predicts a more extended region, which implies an earlier formation of the vortex.

By looking at the cross-flow C_p distribution in the cut plane located at $x/c = -0.35$ (Fig.4.10e) and at $x/c = -0.125$ (Fig.4.10e) we observe two suction peaks. The higher one is associated with the secondary vortex outboard the wing tip, while the other is with the primary vortex above the suction side. At $x/c = -0.35$, the two models predict the same higher peak, while the SST model gives a higher prediction for the second one. At $x/c = -0.125$, the two models predict a similar lower peak, while the maximum peak is higher in the SA-NEG prediction. The surface region (peak width) interested by the two C_p minima in the two predictions is comparable. The same figure also presents the skin friction cross-flow profiles predicted at the same locations of the pressure distribution. Associated with the pressure peaks of $x/c = -0.35$ and $x/c = -0.125$, we observe an increase of the C_f magnitude. No peak is observed at $x/c = -0.9$. At $x/c = -0.35$ the two lines crosses between $-0.10 < z/c < -0.15$, indicating the start of separation. At $x/c = -0.125$ the same point is located further from the wing tip between $-0.15 < z/c < -0.20$. The effects of the Reynolds number at the same span-wise locations can be observed in Fig.???. The main difference are observed at $x/c = -0.35$, where the two models at lower Reynolds predict higher skin friction magnitude peaks. At $x/c = -0.125$, a lower distance is observed between the skin friction profiles of the two flow conditions. At the same location we observe lower suction peaks for $Re = 1.2 \times 10^6$.

Skin friction and static pressure peaks are also observed along the middle of the wing tip in Fig.4.6. The static pressure coefficient steadily rises between $-0.8 < x/c < -0.5$, then a suction peak is observed between $-0.3 < x/c < -0.1$. At the same location, a skin friction coefficient increase is observed. In both cases, the predictions of the SA model are higher. Going to lower Reynolds, we observe lower suction peaks and a slightly higher skin friction coefficient distribution. The peaks of the latter are shifted to the left, indicating a small movement of the converging line.

The effects of the primary vortex on the surface pressure and skin friction distributions can also be observed in Fig.4.12a,b,c,d. The latter presents the stream-wise C_f and C_p profiles predicted by the two turbulence models, taken at $z/c = -0.065$ and $z/c = -0.023$. The pressure coefficient results are compared to the experimental results of Chow, shown in black squares, and the numerical simulations of Churchfield, shown in dotted lines. The latter are obtained using SA and SST models with rotations/curvature corrections (SA-RC and SST-RC). At $z/c = -0.065$, located next to the suction

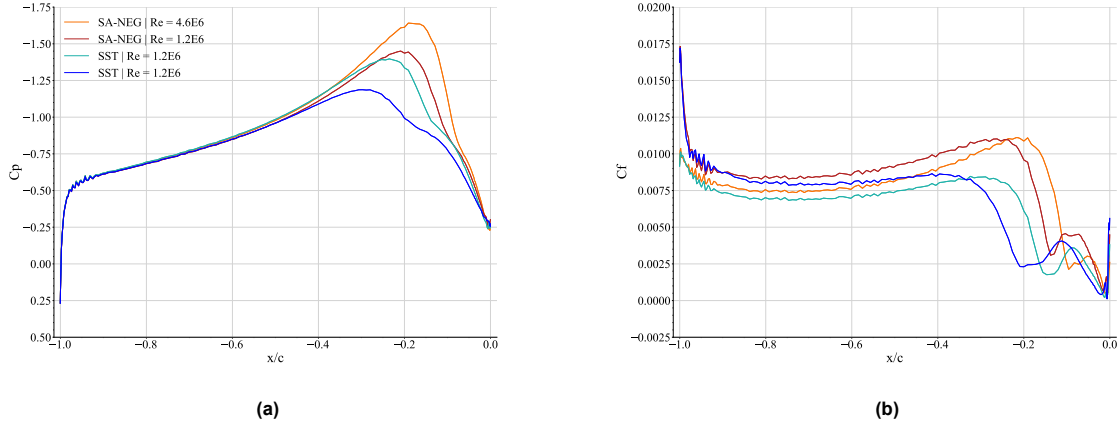


Figure 4.6: Static pressure and skin friction coefficient distribution along the wing tip centerline.

region below the primary vortex, a pressure drop is noted between $-0.2 < x/c < 0$. The SA-NEG and SST predictions are in good agreement with the experimental and numerical results, only slightly under-predicting the pressure drop. More pronounced differences between the models are observed at $z/c = -0.0235$, located in the suction region core. Here the leading edge suction peak reduction is correctly caught by all the models, while the pressure drop, now interesting $-0.4 < x/c < 0$, is under-predicted by the SA-NEG and SST models. We observe that the SST prediction is closer to the experimental results and similar to the SA-RC one of Churchfield. Instead, the SA-NEG model predicts a narrower and higher peak. Looking at the skin friction distribution, both models predicts separation between $-0.8 < x/c < -0.6$ for both span locations. An increase in the coefficient magnitude is noted in the same location of the suction peak. As for the C_p distribution more marked differences in C_f magnitude are observed at $z/c = -0.0235$. Here the SST model predicts a higher skin friction peak between $-0.5 < x/c < 0$.

The effects of the Reynolds number on the two stream-wise skin friction and pressure profiles are shown in Fig.4.12e,f,g,h. At $z/c = 0.625$ no evident differences are observed. At $z/c = 0.675$, going to a lower Reynolds number, both models show a decrease in the pressure drop magnitude. The decrease is more pronounced in the SST predictions. By comparing with the results of Lombard, we observe that the implicit LES profiles are shifted upwards with respect to the SA-NEG and SST profiles at both locations. A possible explanation for this might be a different reference location to define the pressure coefficient. While we use the same reference location of Chow, $x = -1.1344c$, $y = 0.3423c$ and $z = 0.0969$, Lombard provides no information on the reference used. We also observe that at $z/c = 0.675$, the LES computations predict a higher magnitude of the pressure drop caused by the primary vortex. Regarding the skin friction distribution, the profiles are shifted upwards at lower Reynolds. The separation location is still predicted between $-0.8 < x/c < -0.6$, and a slightly higher skin friction peak is observed at $z/c = -0.065$ between $-0.4 < x/c < 0$.

The total lift and drag of the wing, obtained by numerically integrating the surface pressure, are reported in Tab.4.1. We observe that the C_L and C_D prediction of the various simulations are comparable, with an 11% increase in the drag coefficient going to lower Reynolds simulations. The maximum difference in the lift coefficient concerning the experimental results of Chow is 11.7%. We observe that the difference may be linked to the inviscid condition used for the tunnel wall at which the wing is attached. In the experimental results, a horseshoe vortex is observed at this location, which is not represented by the numerical simulations.

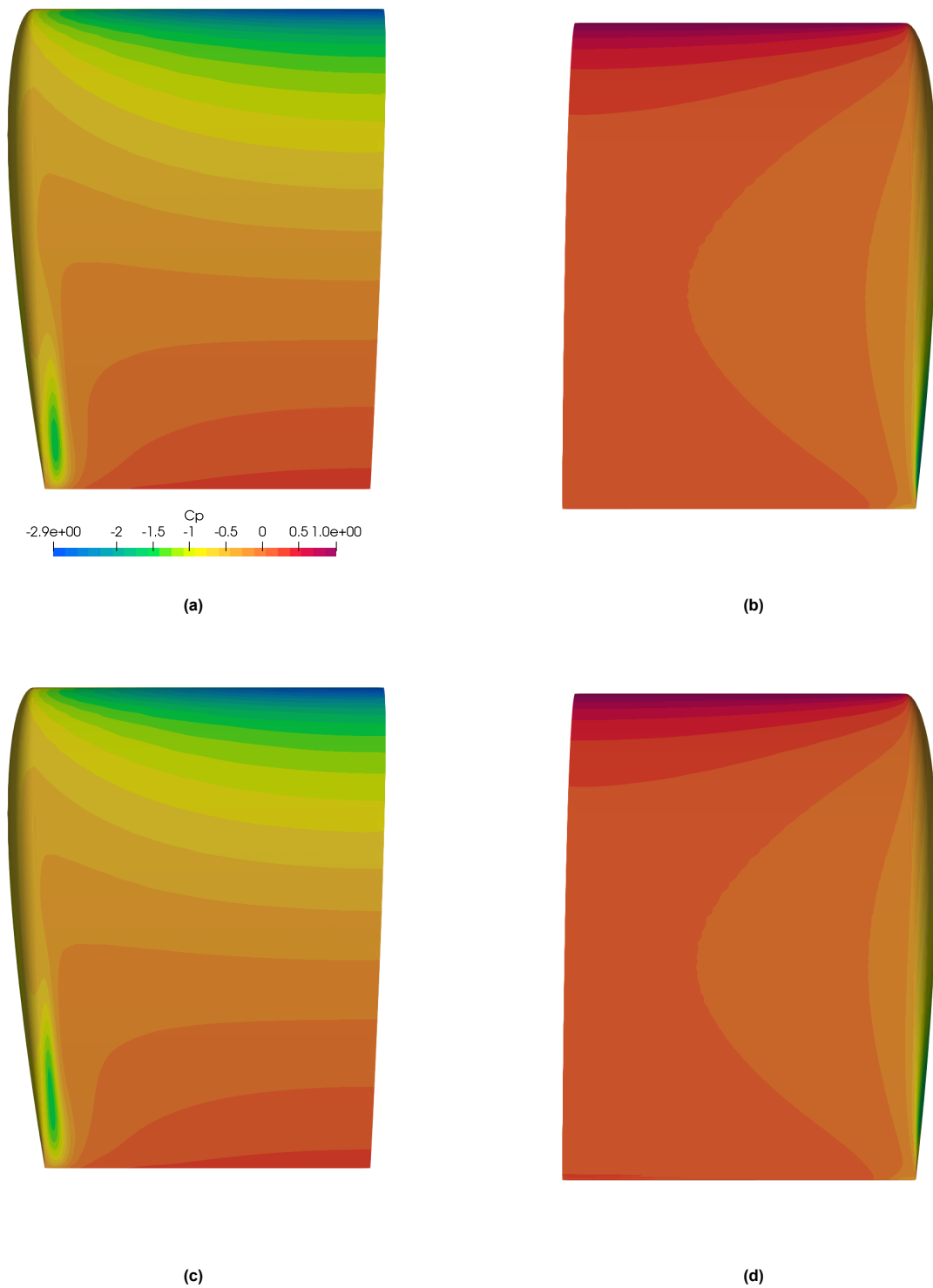


Figure 4.7: Surface static pressure coefficient contours. (a) Suction side SA-NEG model. (b) Pressure side SA-NEG model. (c) Suction side SST model. (d) Pressure side SST model.

Test Case	Reynolds Number	C_L	C_D
SA-NEG	4.6×10^6	0.559	0.051
SST	4.6×10^6	0.57	0.052
SA-NEG	1.2×10^6	0.569	0.057
SST	1.2×10^6	0.569	0.057
Chow et al.	4.6×10^6	0.51	-

Table 4.1: Total lift and drag of the wing as predicted by the numerical simulations and experiment. Churchfield and Lombard simulations do not compare in the table because they do not provide any values for these quantities. Chow only provides an estimation of the C_L .

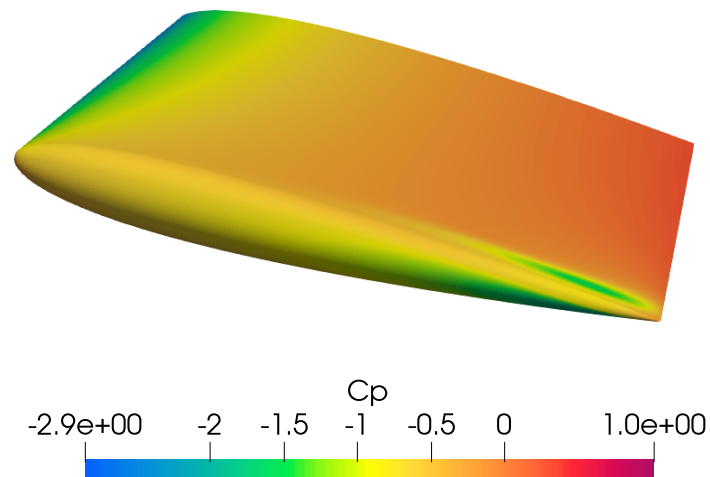


Figure 4.8: Surface static pressure coefficient.

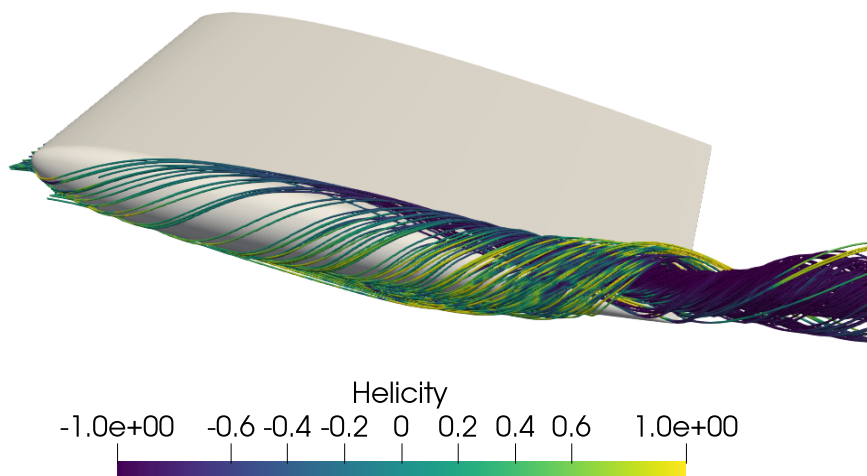


Figure 4.9: Vortex visualization using three-dimensional streamlines extracted from the velocity field. The streamlines are colored by the normalized helicity, defined as inner dot product of velocity and vorticity vectors, $H = (\mathbf{U} \cdot \boldsymbol{\omega}) / (|\mathbf{U}| |\boldsymbol{\omega}|)$. This physically represents the angle between the velocity and vorticity fields, and it helps to visualize the vortex core (characterized by the alignment of the two vectors). In this case, one can notice that the vortex core, in dark blue, is placed on the lower rear part of the wing tip directly above the suction side.

4.2. Vortex formation and propagation

As gathered by the results of Sec.4.1, the flow over the wingtip develops into a highly skewed three-dimensional boundary layer that rolls up and detaches into a rapidly rotating vortex. As reported by Chow, the vortex core is characterized by an increasing low-pressure region that gradually accelerates the fluids entering into a jet-like behavior. A turbulence model is supposed to accurately predict the boundary layer roll-up on the wing surface and the vortex evolution in the near field downstream.

A typical way to analyze the performance of the RANS models in this context is to study the evolution of the mean quantities along the vortex centerline. However, we first need to define how the latter is identified.

4.2.1. Vortex centerline identification

Although the notion of vortex is widely used in fluid dynamics, no definitive and unambiguous definition exists to describe it. As an example, vortices are often identified as regions of high vorticity. However, no universal threshold exists over which vorticity is considered high. Moreover, vorticity may also be high in flows where no vortices are present, as in parallel shear flows. Therefore it is not surprising that the three literature references define the vortex centerline in different ways.

Chow identifies the vortex center as the point of local minimum cross-flow velocity. The centerline is then defined by considering several cutting planes with a stream-wise normal direction and computing the vortex center for each. The union of the different centers defines the centerline segments. Lombard uses the same method to determine the centerline. However, the vortex center is identified as the point of local pressure minimum. Instead, Churchfield favors an automated algorithm based on the velocity gradient tensor eigen-analyses. The algorithm is fully described in [44]. It firstly identifies throughout the mesh regions of swirling flow, characterized by a pair of complex eigenvalues and a real one. To compute the eigenvalues of the tensor, all the mesh elements are broken into tetrahedra (if not already of this element type) since they have precisely the correct amount of grid points to compute a unique velocity gradient tensor (constant over the entire element). If swirling, the direction orthogonal to the spiral plane, associated with the real eigenvalue, is used as the swirl axis. This direction is subtracted

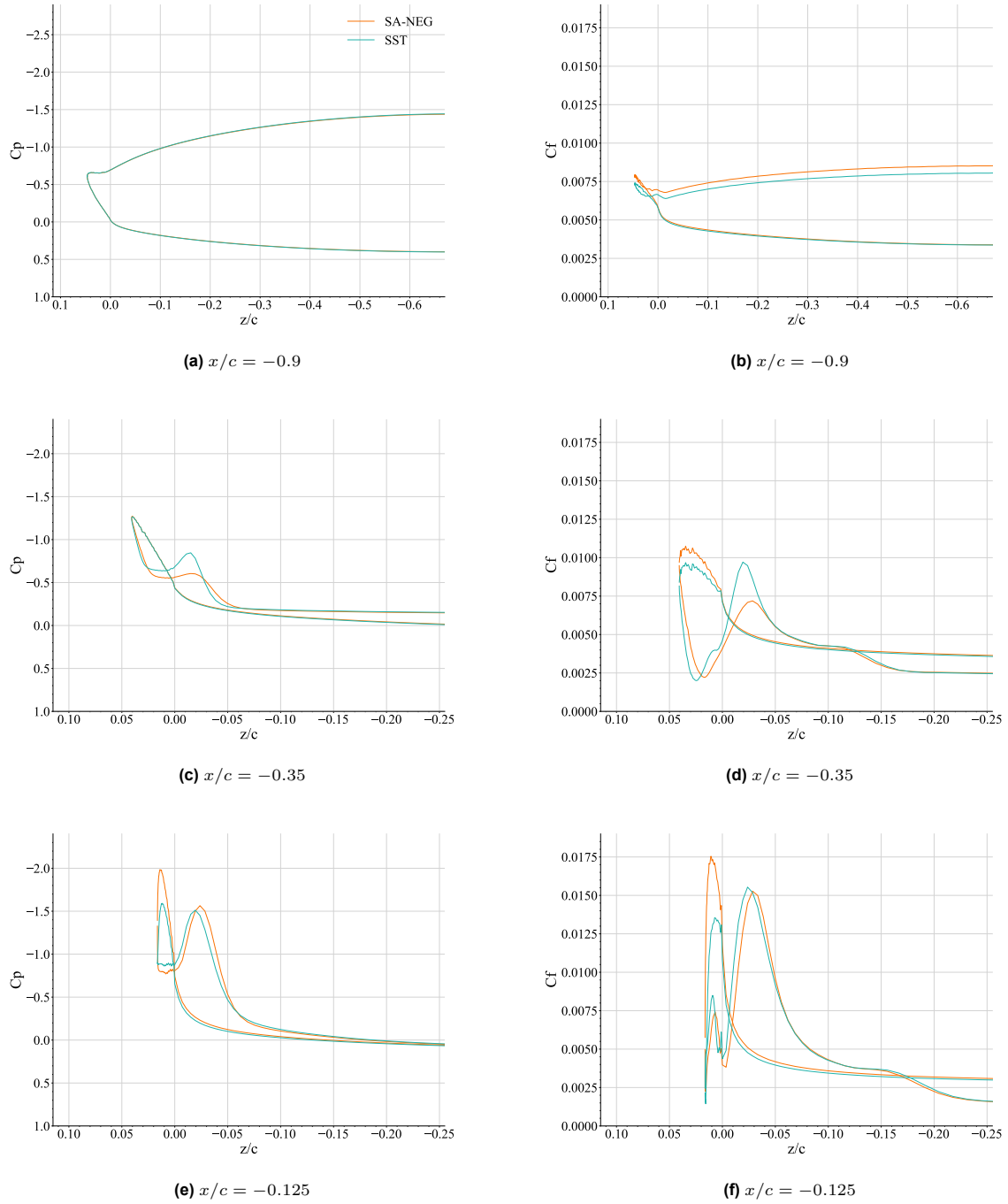


Figure 4.10: Cross-flow skin friction coefficient magnitude C_f and static pressure coefficient C_p distribution at three stream-wise locations.

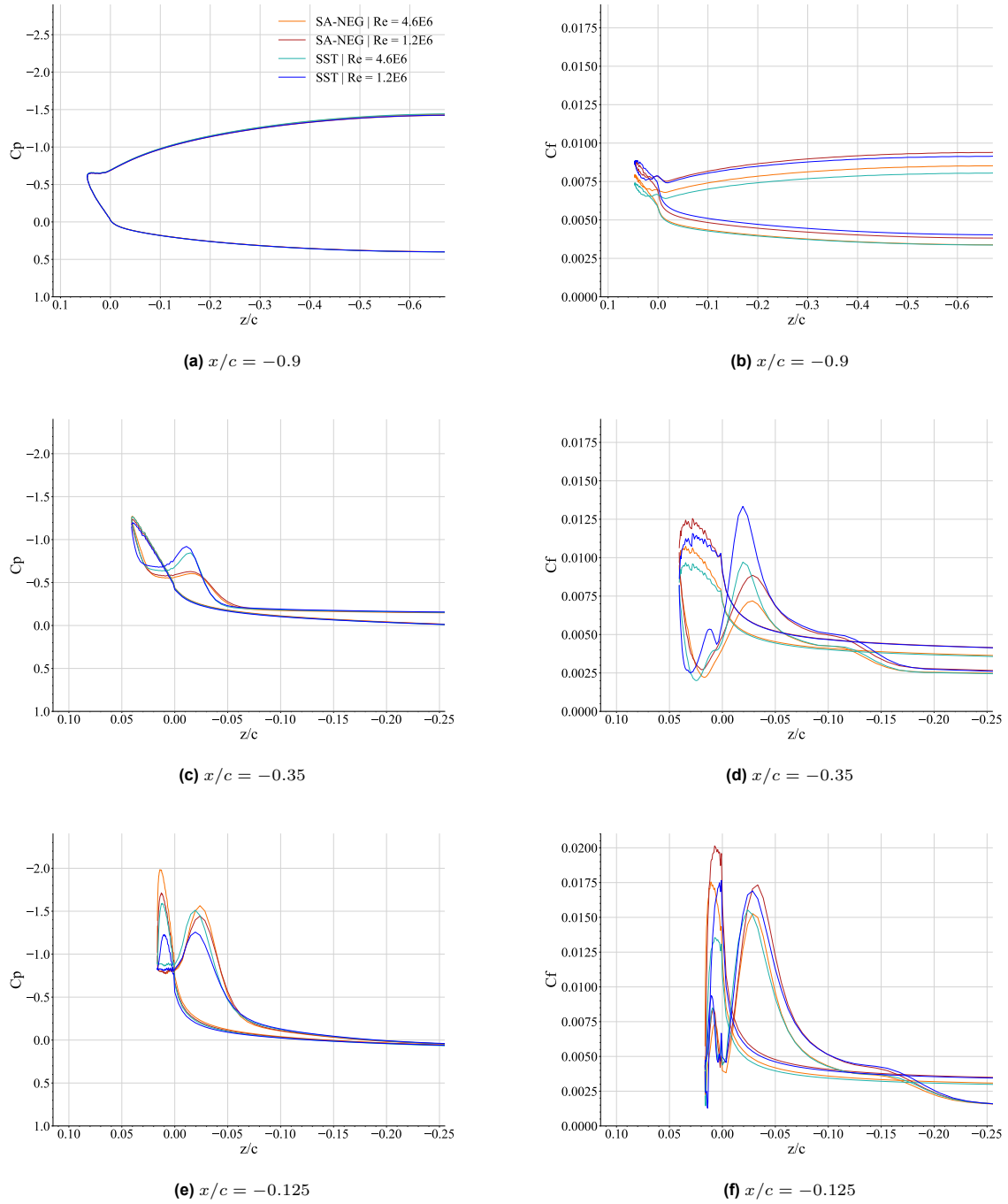


Figure 4.11: Cross-flow skin friction coefficient magnitude C_f and static pressure coefficient C_p distribution at three stream-wise locations for different Reynolds.

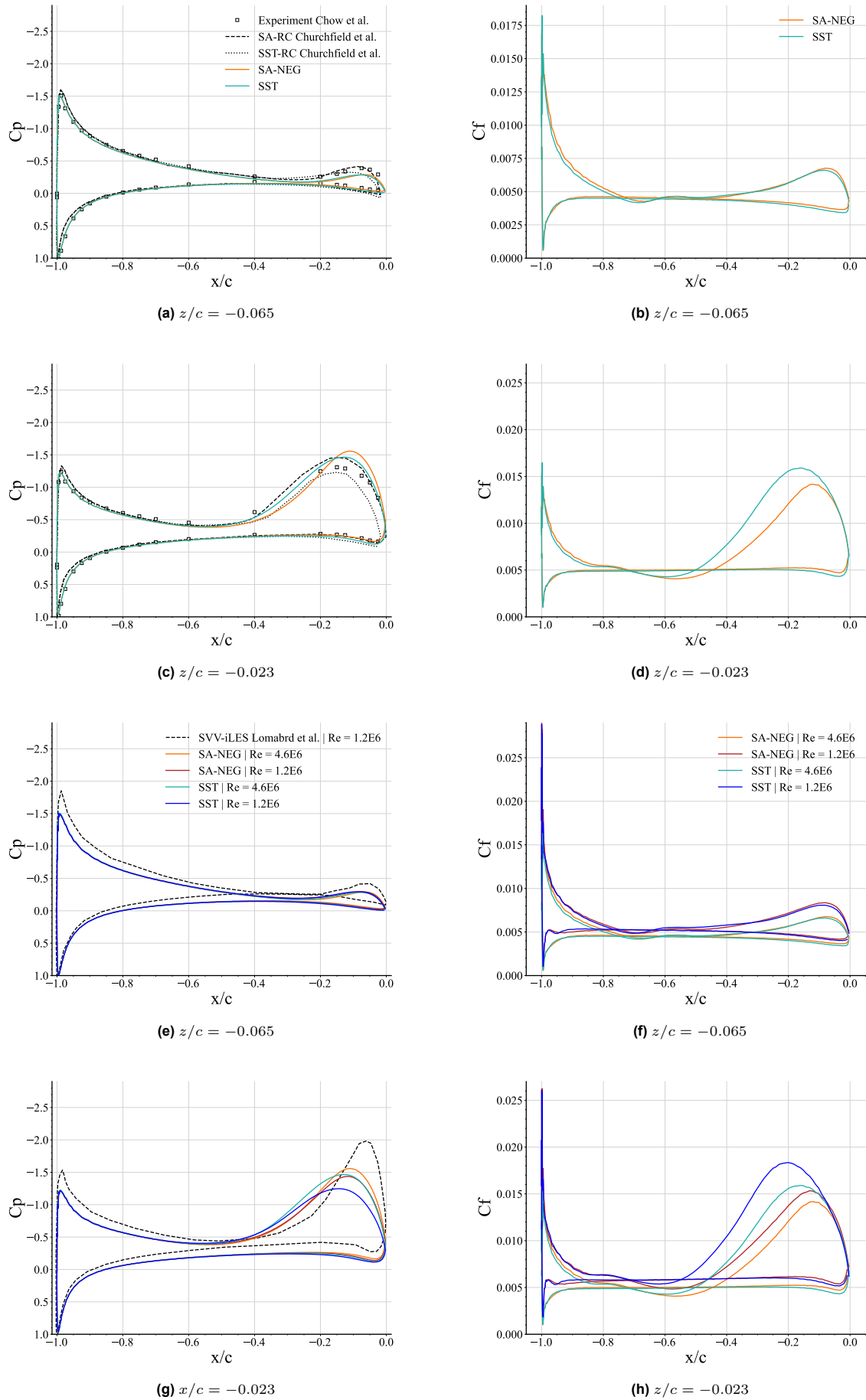


Figure 4.12: Stream-wise skin friction coefficient magnitude C_f and static pressure coefficient C_p distributions at two span-wise locations. (a), (b) compares the pressure profiles with the reference results of Churchfield and Chow. (e), (f), (g), (h) compares with simulations done at lower Reynolds number and with the reference results of Lombard.

from the nodal velocities, and if the resulting reduced velocities are equal to zero in the element face, the latter is marked. With two or more marked faces on the element, the vortex centerline has pierced the cell. These lines are then collocated and drawn to display the core segments. The algorithm is implemented in the visualization software Paraview by an external plugin called "VCG vortex centerline", which can be found in [48].

Although automated, Churchfield centerline identification still requires manual tuning and adjustments since regions of swirling flow can also be detected in secondary vortices and in the formation of boundary layers. Instead, the methods used by Chow and Churchfield may be sensible to the cutting plane choice. In particular, we observe that two choices can be made: use planes with normal direction aligned to the stream flow (vertical planes) or aligned to the wing mean chord (orthogonal planes), which in this case is inclined by 10° . To define the best method to use, we analyzed the sensitivity to the plane choice of the pressure minimum method in Fig.4.13a and 4.13b and cross-flow minimum in Fig.4.13c and 4.13d, with respect to the centerline position prediction. Then in Fig.4.13e and 4.13f we compare their results (found using vertical planes) with the ones obtained using the VCG plugin. While the minimum pressure method is independent of the plane choice, the cross-flow technique provides different predictions between $-0.4 < x/c < -0.1$, depending on the plane inclination. The minimum pressure centerline identification results are also comparable to the ones of the VCG algorithm. The method used by Lombard seems to be the best choice since few manual adjustments are required in this test case, and the results do not depend on the choice of vertical or orthogonal planes. Therefore, we adopted the same centerline identification procedure to study the mean quantities evolution along the vortex core.

4.2.2. Vortex centerline mean quantities evolution

Fig.4.14 reports the evolution of the principal mean quantities along the vortex centerline. Fig.4.14a,b,c,d compares the results of the SA-NEG and SST models against the reference results of Chow and Churchfield.

All the models give centerline location predictions in good agreement with the experimental results of Chow, with a maximum discrepancy on the y location between $0 < x/c < 0.2$. In particular, we observe that the SST model performs better in the y-position prediction than the same model with rotation corrections. While the SA model span-wise centerline location is the closer to the experimental results, with the SST model that predicts a more straight movement of the core. The SST prediction of the static pressure coefficient is close to the experiment between $-0.3 < x/c < -0.1$, then between $0 < x/c < 0.6$ it predicts a repressurization of the vortex core, which is in disagreement with the experimental results. A similar behavior is also observed in the SA-NEG model and in the u/U_{ref} plot, where both models predict a sharp decrease of the axial velocity after $x/c = -0.1$. The distance between the models and the experimental results is connected to the Boussinesq hypothesis. As shown in the viscosity ratio distribution ν_T/ν in Fig.4.15, the region downstream the wing is dominated by the eddy viscosity, which acts as an additional viscosity diffusing the mean quantities.

A similar behavior is observed in the u/U_{ref} . Both models predict a sharp decrease after $x/c = -0.1$, which disagrees with the experimental results. The results obtained at a lower Reynolds, Fig.4.14e,f,g,h, show similar behavior. The centerline position prediction is very similar to the higher Reynolds one. However, we observe that the results of Lombard predict a slightly lower vertical center position. The static pressure coefficient and axial velocity evolution is comparable to the one obtained at higher Reynolds, with the curves slightly shifted downwards (in the C_p plot) and upward (in the u/U_{ref} plot) after $x/c = -0.1$.

Fig.4.15 also shows the distributions of the total pressure coefficient and the adimensional Reynolds stress norm. Where the first is defined as:

$$C_{p0} = \frac{P_0 - P_{0_{ref}}}{0.5 \rho_{ref} U_{ref}^2} \quad (4.1)$$

with $P_0 = P(1 + \frac{\gamma-1}{2} M^2)^{\frac{\gamma}{\gamma-1}}$ the total pressure, and the Reynolds stress norm distribution is defined as:

$$\| \langle u'_i u'_j \rangle \| = \sqrt{\sum_i \sum_j \langle u'_i u'_j \rangle^2} \quad (4.2)$$

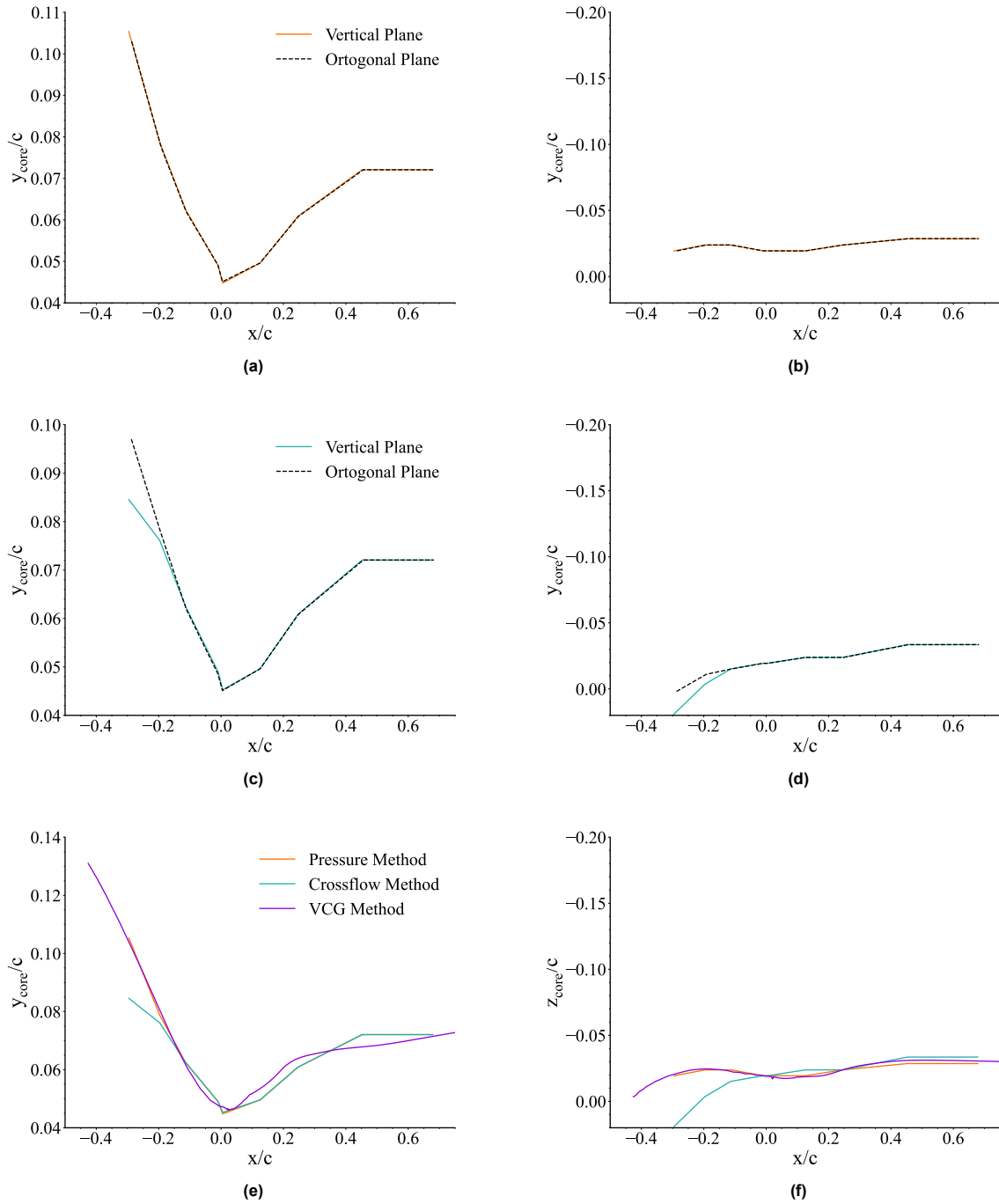


Figure 4.13: Centerline position prediction for different identification methodologies.

with $\langle u'_i u'_j \rangle$ defined using the Boussinesq hypothesis. The norm is then adimensionalised by the square of the reference velocity. We observe that total pressure losses characterize the core vortex region over the wing. Then downstream, the wing C_{p0} tends to rise gradually due to the increasing importance of the eddy viscosity. The latter causes momentum transfer from the exterior streamwise flow to the vortex core, reducing the gradients in this region. Downstream the wing, we also observe a decrease in the Reynolds stress norm. We observe that the very low values of the latter in the central vortex region are connected to the symmetries in the stress pattern, which can be better seen in Fig.4.22.

4.2.3. Vortex development in the near wake

From the skin friction field visualization, we observed that the RANS models correctly reproduce the main topological flow feature over the surface, notably the open-separation and the primary and secondary vortex formation. Fig.4.16 gives a better view of the vortical structures predicted by the SA-NEG model. Two vortices can be clearly observed, separated by the saddle point. The stream-wise vorticity visualization is particularly interesting. We can clearly observe the shear layer departure from the surface toward the vortical structures.

As seen in the previous section, the RANS models also give centerline location predictions in good agreement with the experimental results of Chow. It is now interesting to compare the vortex shape predicted by the RANS with the experimental and numerical reference data. The cross-flow field streamlines predicted by the SA-NEG model at $x/c = -0.115$ (Fig.4.16) are in good agreement with the results of Lombard, shown in Fig.4.17, which, however, predict a more isotropic round shape of the vortex. We observe that the shape of the experimentally obtained vortex is closer to the one of the RANS computations. However, the experiment streamlines do not show the secondary vortex. One explanation is the probe spacing, which is not refined enough to be able to represent the secondary structures.

More similar to the reference results (Fig.4.19) are the cross-flow streamlines computed at $x/c = 0.452$. Here, the experimental results of Chow report a kink of the vortex, which is believed to be caused by the presence of a secondary vortex orbiting around the primary one. The evidence of this secondary vortex can be seen in both cross-flow fields of Chow and Lombard as flat spots in the cross-flow streamlines. The latter are spot between $0.01 < y/c < 0.07$ and $0.03 < z/c < 0.06$ in the experimental results and $0.06 < y/c < 0.1$, $0.03 < z/c < 0.06$ in the LES simulations. These flat spots can also be seen in the SA-NEG predictions between $0.04 < y/c < 0.07$, $0.03 < z/c < 0.06$. More interestingly, looking at the stream-wise vorticity distribution in Fig.4.20, one can notice a weaker, counter rotating vortex associated with the region interested by the vortex kink.

Similar cross-flow field visualizations were obtained for the SST model. They are not shown for brevity.

4.3. Reynolds stress evolution in the near wake vortex

In his paper, Chow used three hot-wire anemometers to measure turbulent fluctuation in the flow field over the wing and downstream. He reported significant levels of all three anisotropic Reynolds stress components in the vortex and misalignment with their corresponding strain rate components. The offset of the two tensors is observed to be more pronounced with the downstream distance.

By comparing the Reynolds shear stresses predicted by the SST model at $x/c = 0.452$ in Fig.4.22 with Chow's experimental results, shown in Fig.4.21, we clearly observe that, in the RANS simulations, $\langle u'v' \rangle$, $\langle u'w' \rangle$ and $\langle v'w' \rangle$ align themselves with the corresponding mean strain rate, completely loosing the misalignment observed in the experiment. However, we observe that the linear eddy viscosity model predicts the same two-lobe pattern of $\langle u'v' \rangle$, $\langle u'w' \rangle$ and four leaf pattern of $\langle v'w' \rangle$. Similar results were obtained from the SA-NEG model. No further analyses were possible due to the absence of additional data, given the experimental results. We further observe that, in his work, Churchfield also reports a failure of the misalignment prediction of the SA and SST model with rotation correction.

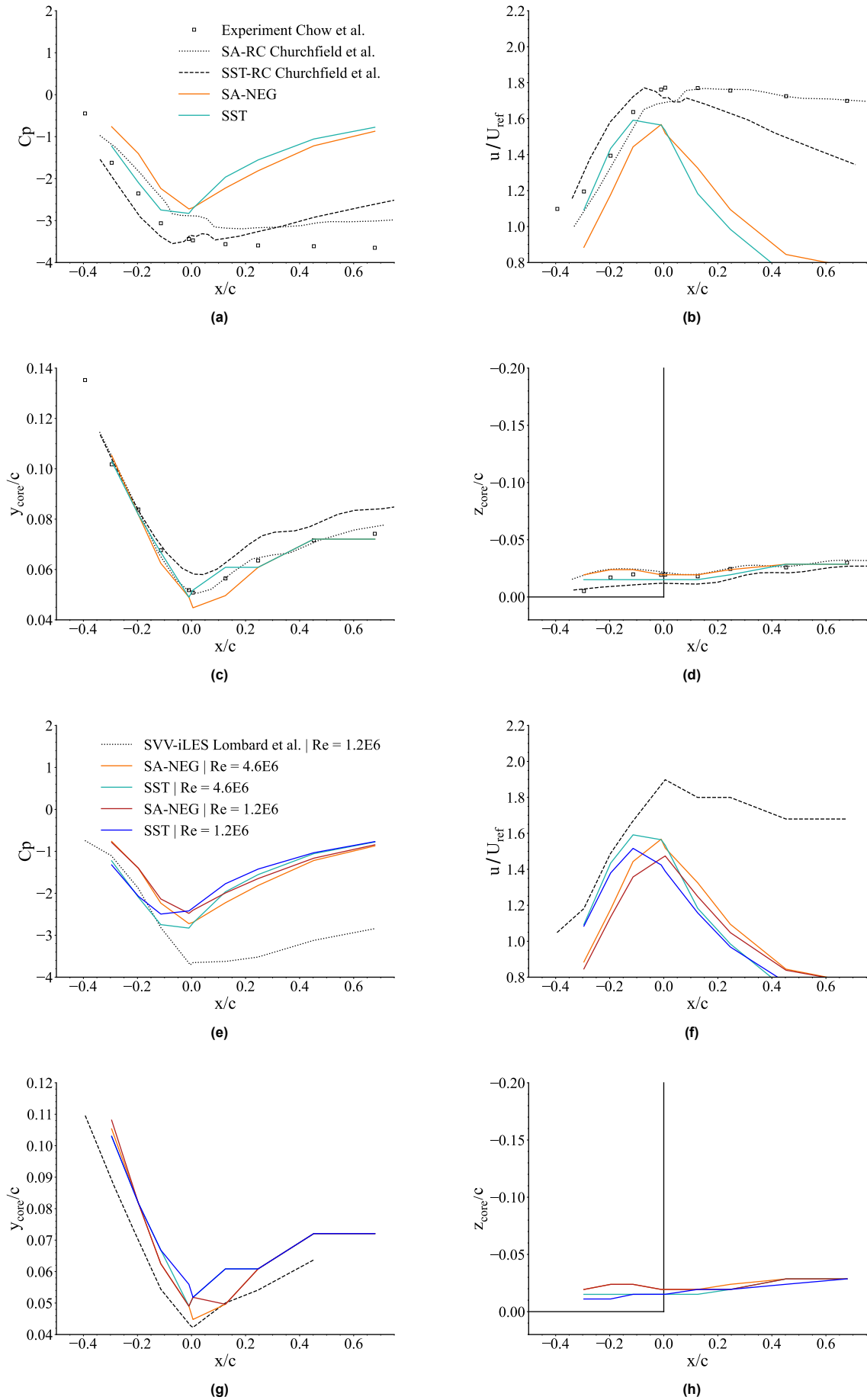


Figure 4.14: Flow means quantities evolution along the cortex centerline. In (d) and (h), the continuous black line illustrates the wing position.

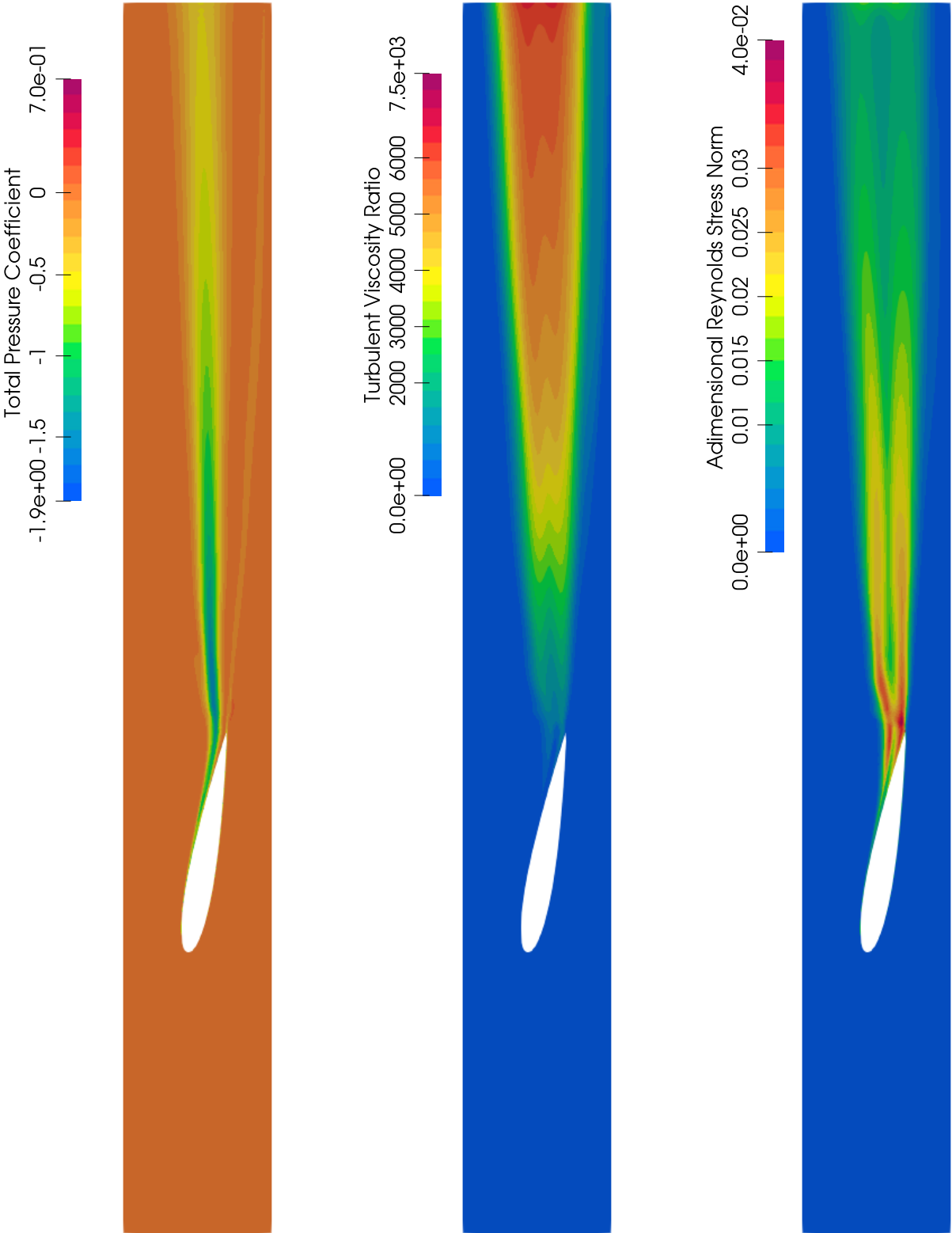


Figure 4.15: Total pressure coefficient, turbulent viscosity ratio and adimensional Reynolds stress norm distribution along the xy plane located at $z/c = -0.015$.

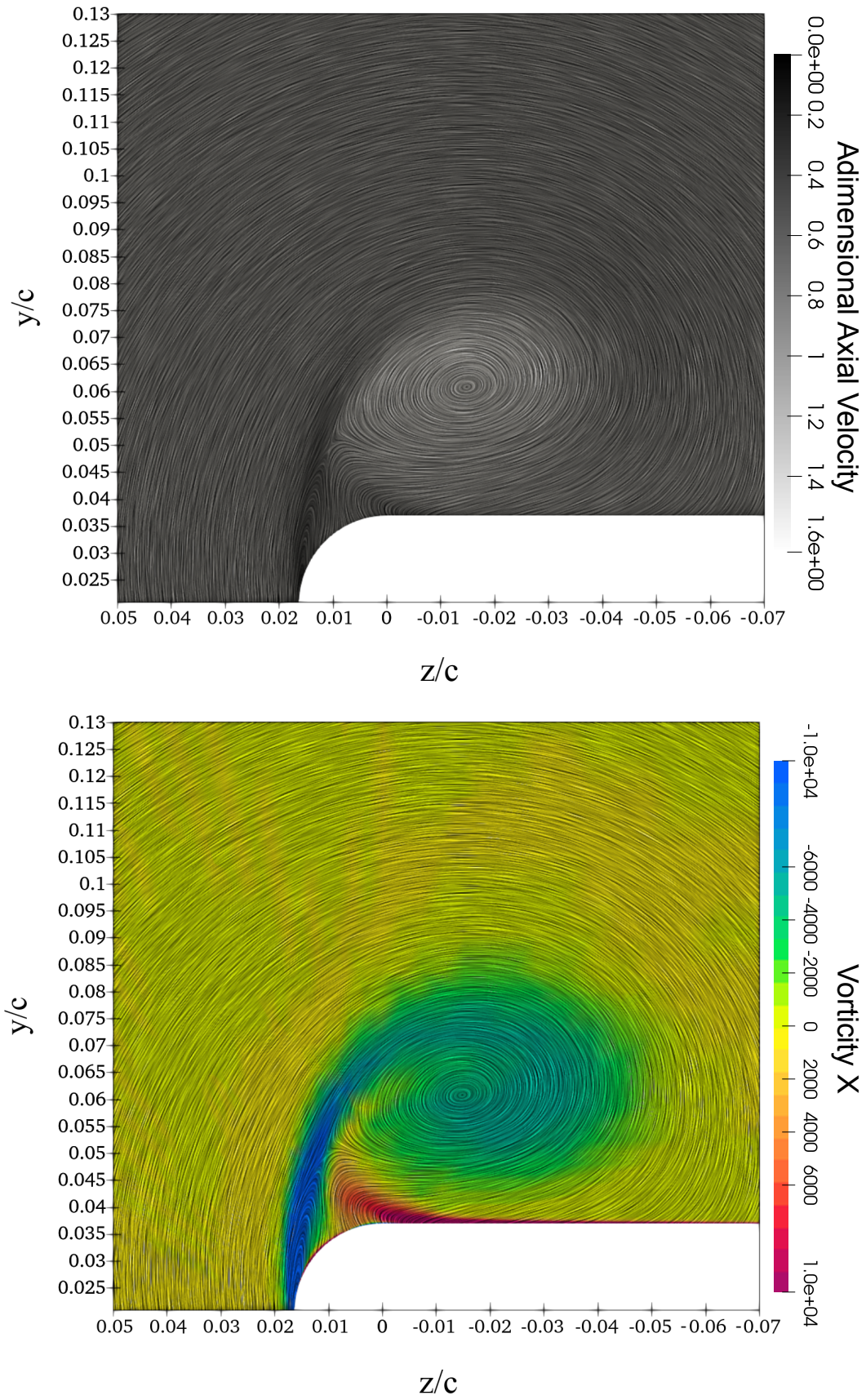
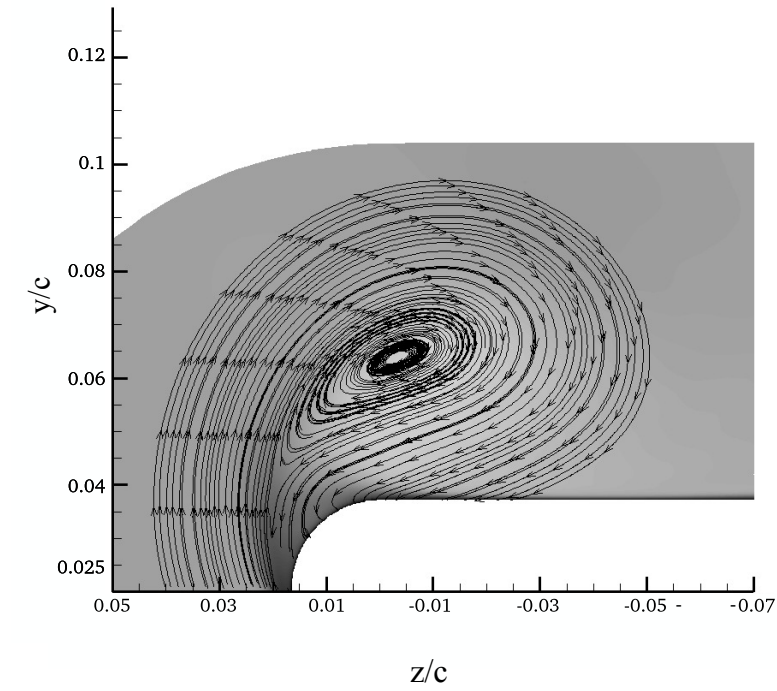
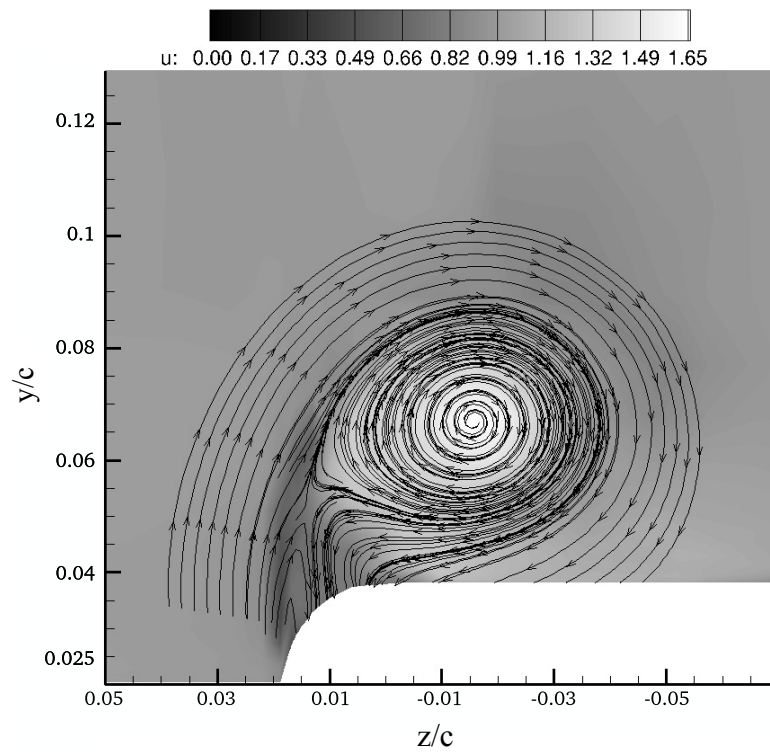


Figure 4.16: Cross-flow field streamlines at $x/c = -0.115$ obtained using line integral convolution visualization in Paraview, colored by the adimensional axial velocity u/U_{ref} on top, and the stream-wise vorticity vector component $\omega_x = \left(\frac{\partial u_z}{\partial y} - \frac{\partial u_y}{\partial z} \right)$ on the bottom.



(a) Chow experiment.



(b) Implicit LES Lombard.

Figure 4.17: Cross-flow field streamlines at $x/c = -0.115$ computed by Chow in (a) and Lombard in (b), taken from [23]. The axes were translated to coincide with the ones used in the present work.

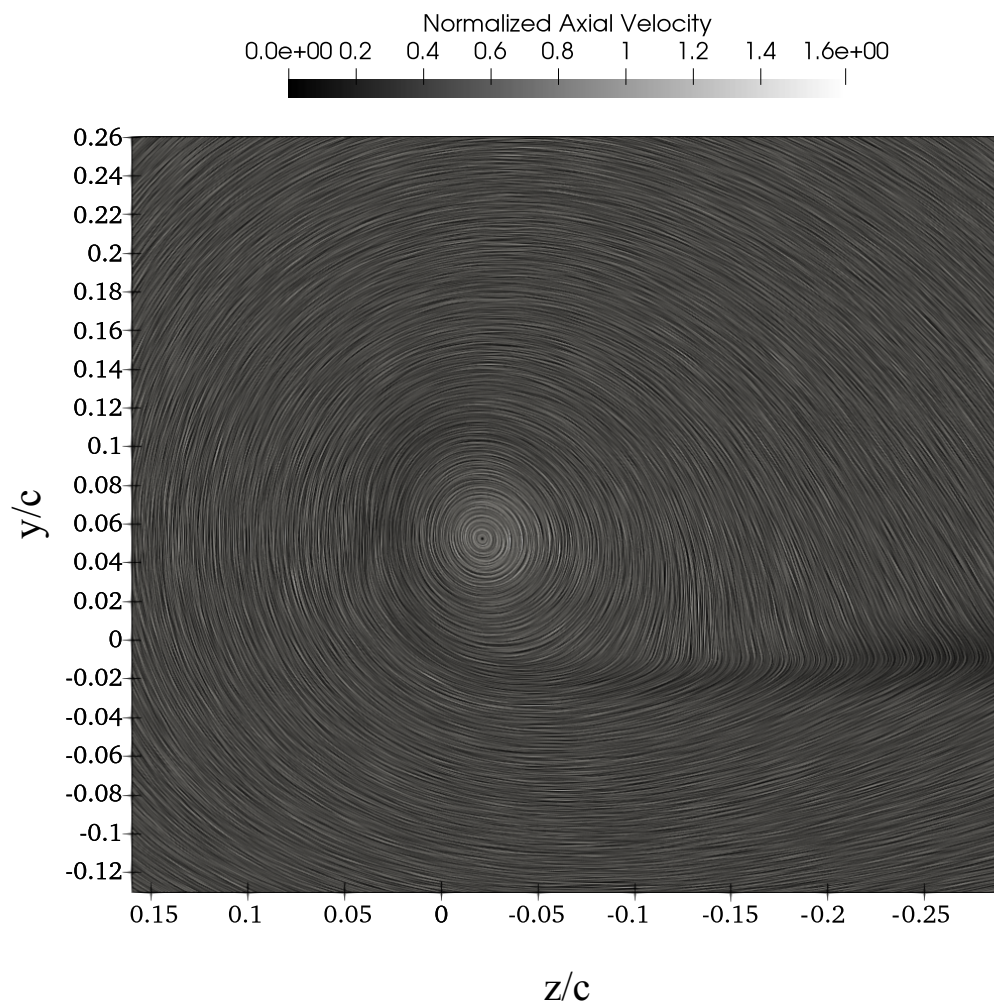
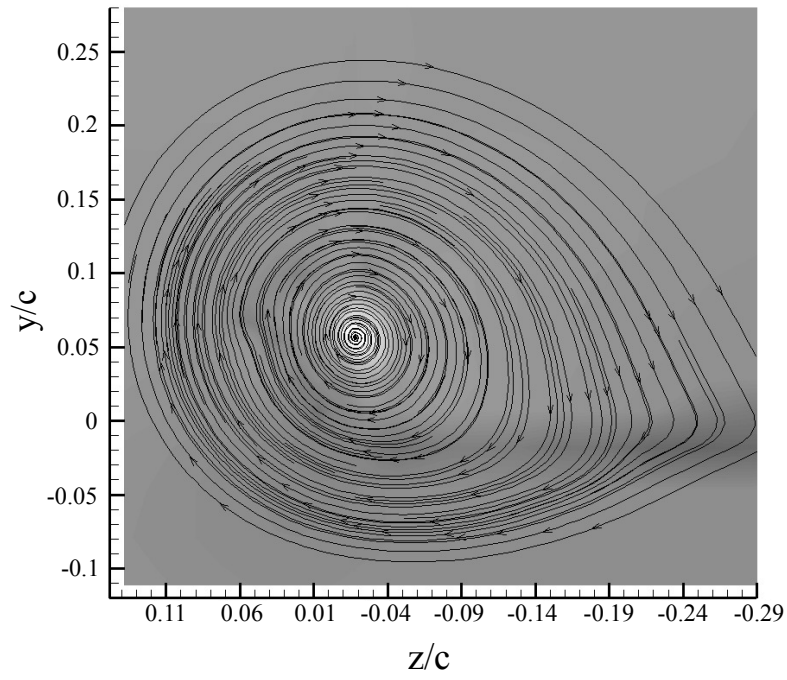
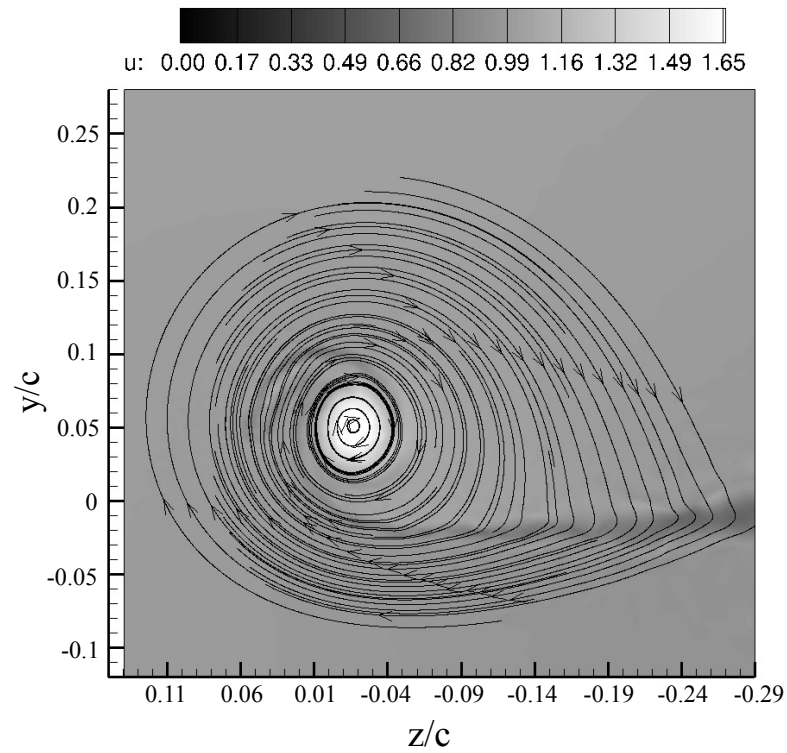


Figure 4.18: Cross-flow field streamlines at $x/c = 0.450$ obtained using line integral convolution visualization in Paraview, colored by the adimensional axial velocity u/U_{ref} .

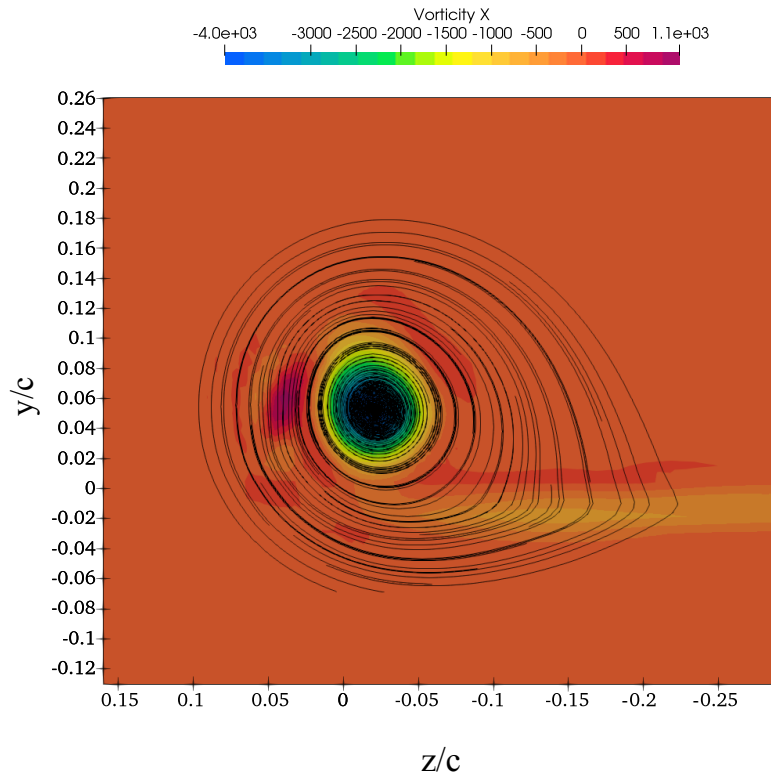


(a) Chow experiment.

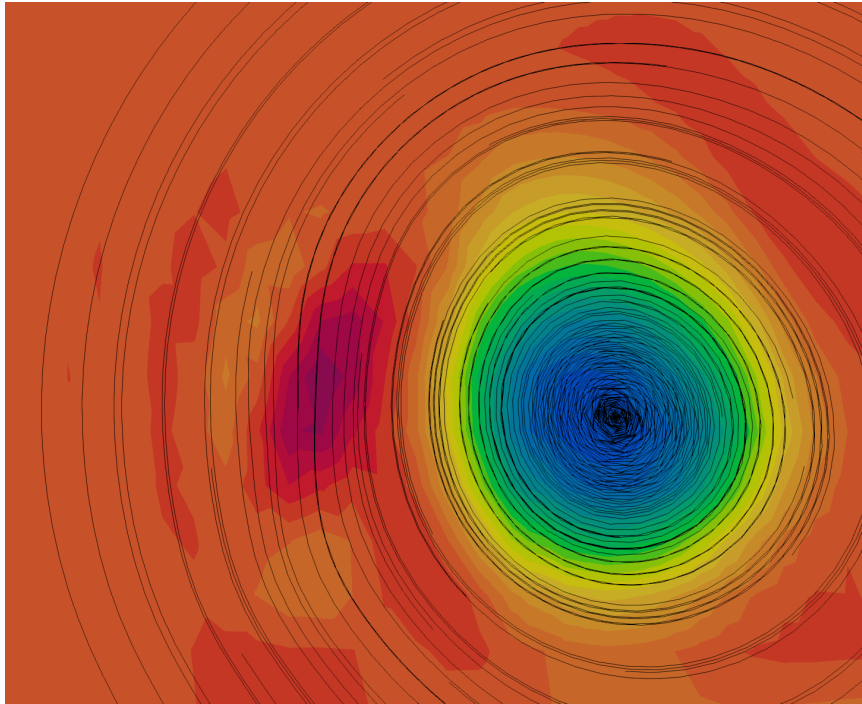


(b) Implicit LES Lombard.

Figure 4.19: Cross-flow field streamlines at $x/c = 0.450$ computed by Chow in (a) and Lombard in (b), taken from [23]. The axes were translated to coincide with the ones used in the present work.



(a)



(b)

Figure 4.20: Cross-flow field streamlines at $x/c = 0.450$, colored by the the stream-wise vorticity vector component $\omega_x = \left(\frac{\partial u_z}{\partial y} - \frac{\partial u_y}{\partial z} \right)$. To better visualize the vortex kink, (b) shows a close-up of (a) near the primary vortex.

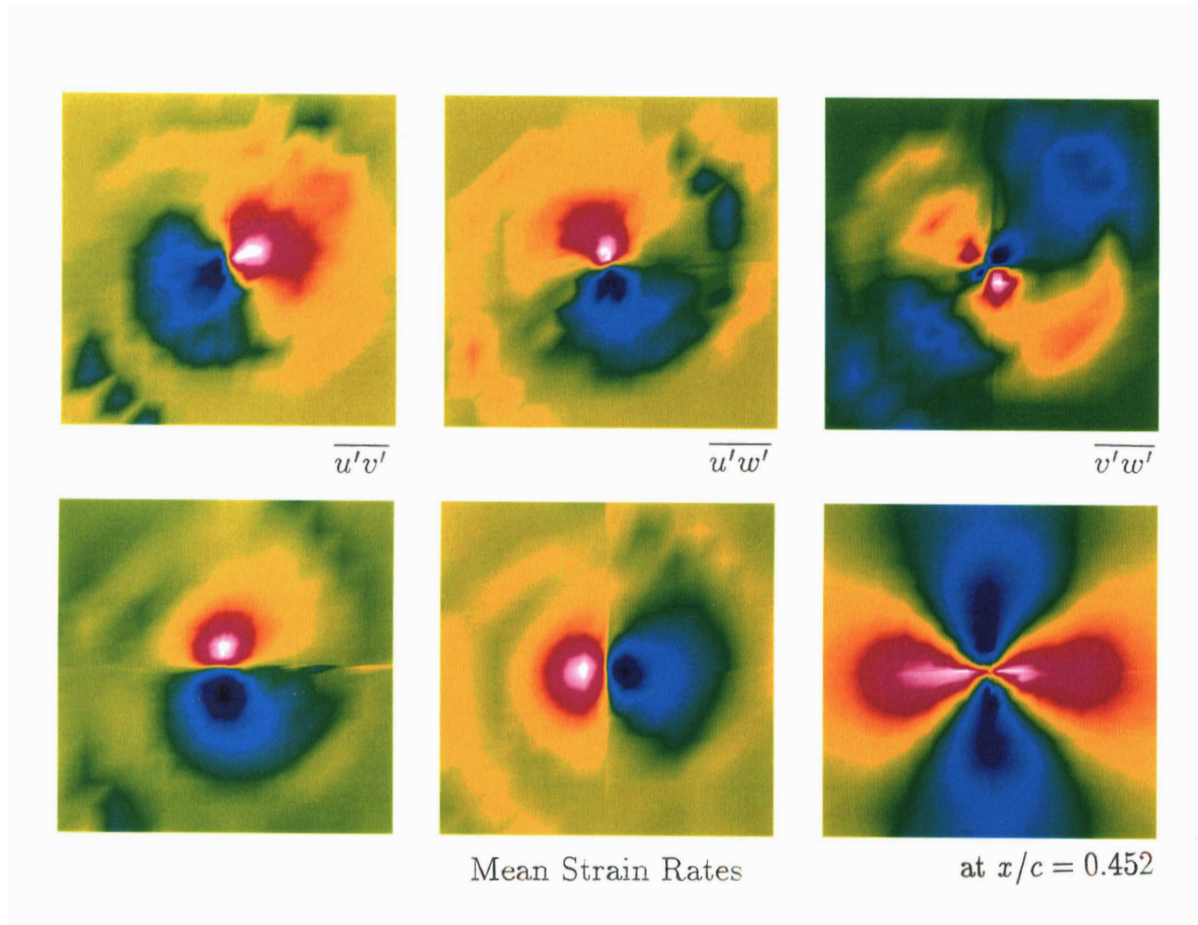


Figure 4.21: Reynolds shear stresses and mean strain rates measured by Chow at $x/c = 0.452$, taken from [7].

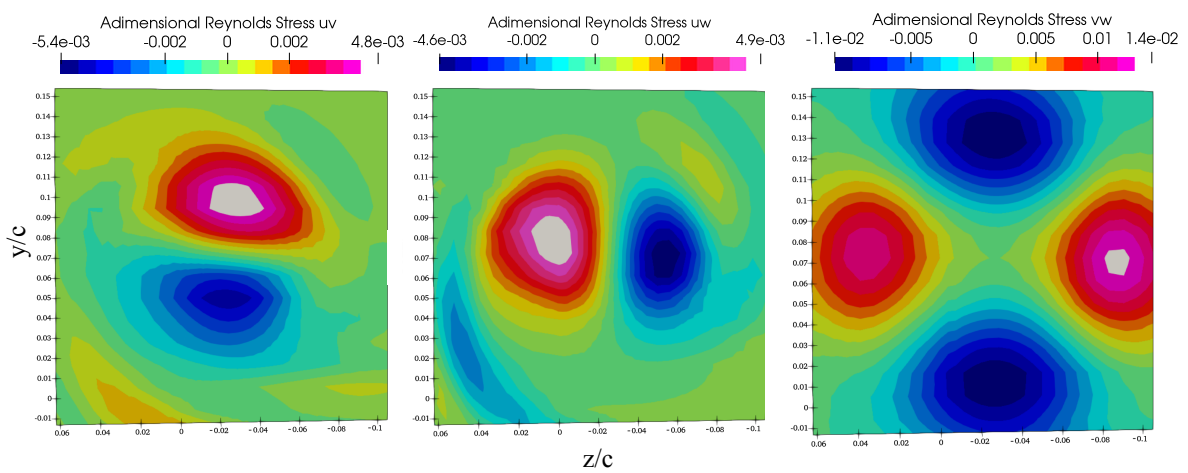


Figure 4.22: Reynolds shear stresses predicted by the SST model at $x/c = 0.452$.

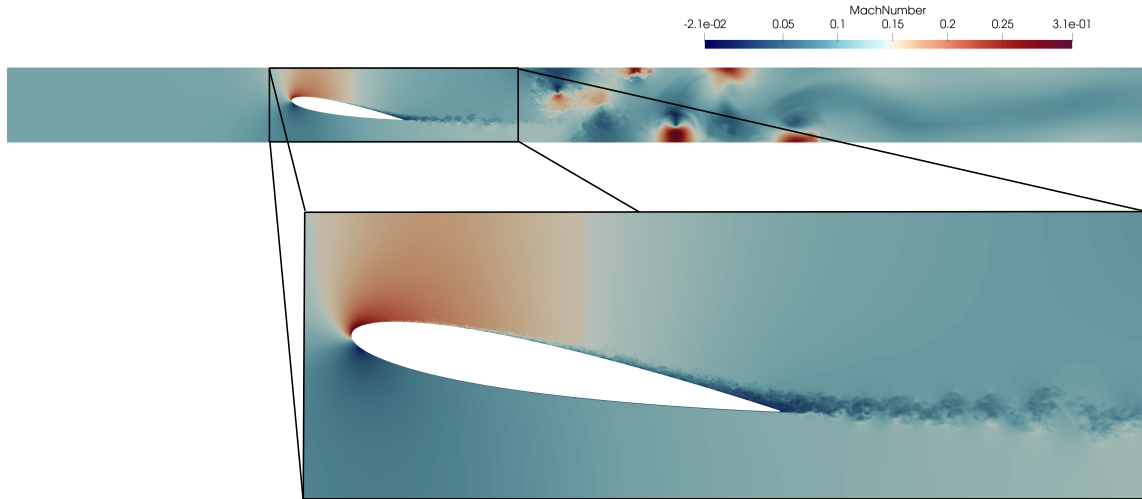


Figure 4.23: Instantaneous Mach number visualization on the domain periodic boundary at $t = 0.074s$.

4.4. LES computations

In this section, we will give a qualitative overview of the instantaneous flow surrounding the extruded airfoil, which will be helpful in the future development of the work. Due to the high computational requirements, it was not possible to have a steady-state simulation to analyze in the present work. Fig.4.23, 4.24 and 4.25 presents the results obtained. After 265 hours of computations, using 1152 CPUs in parallel, we were only able to simulate $0.074s$ of flow evolution, corresponding approximately to two through-flow times (time required by the flow to cross one chord length). We observe that the transient solution, coming from the flow initialization, is still present in the domain, only at one chord length distance from the airfoil.

Nevertheless, the flow around the airfoil appears well established, with a Kármán vortex street clearly visible downstream of the airfoil. The pressure and velocity gradients around the airfoil appear to be entirely included in the structured boundary layer mesh. The boundary layer grows going toward the trailing edge. However, no severe separation is observed. Considering the span-wise velocity and vorticity components on the surface, shown in Fig.4.26 we observe that the boundary layer transition on the suction side occurs very close to the leading edge, while no transition is observed on the pressure side.

The flow visualization suggests that the highly refined unstructured mesh region around the airfoil could be reduced to the vortex region shedding from the trailing edge. This would allow to increase the number of elements in the structured boundary layer mesh, reducing x^+ , without increasing the computational cost. Additionally, the computational domain length could be reduced by introducing a sink term at the outflow to prevent instabilities. This would also save computational resources and discharge the transient solution more rapidly.

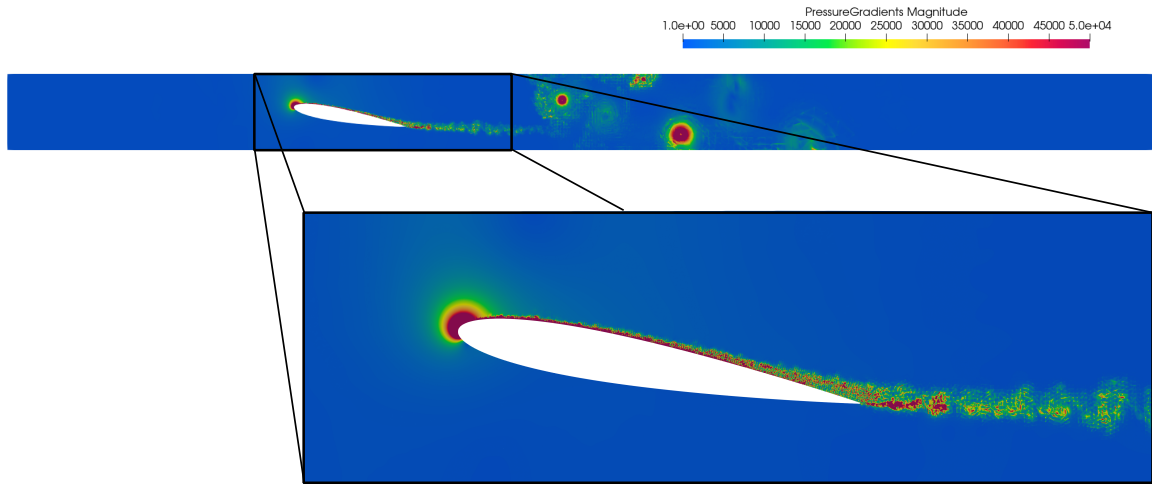


Figure 4.24: Instantaneous pressure gradients visualization on the domain periodic boundary at $t = 0.074s$.

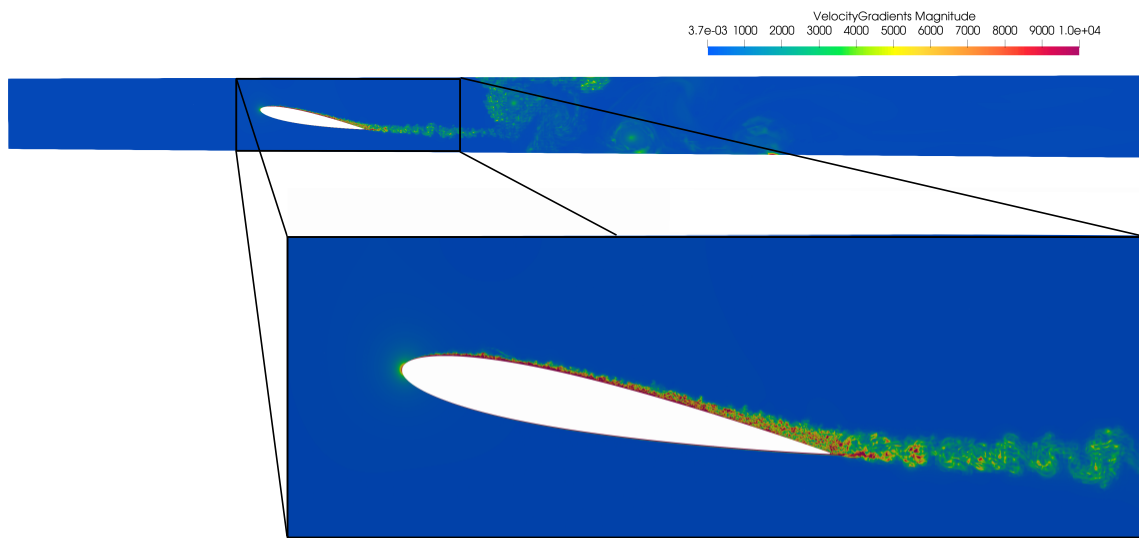


Figure 4.25: Instantaneous velocity gradients visualization on the domain periodic boundary at $t = 0.074s$.

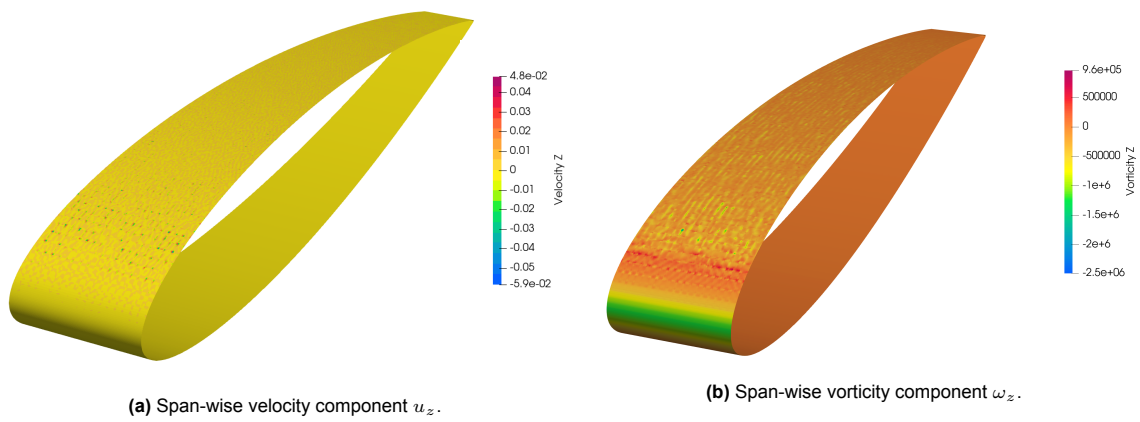


Figure 4.26: Span-wise velocity and vorticity components on the extruded airfoil surface at $t = 0.074s$.

5

Further discussion and future work indications

Although we could not fulfill the project's initial objective, failing to compute the entire wing's LES simulation, we still can provide indications of possible future work based on the comparison with the reference experimental and numerical data.

Key points must be addressed to improve the turbulence closure using a machine learning approach. First, one should define the "learning strategy" to use. During the learning process, the algorithm determines how to define the model that best approximates the given inputs' output. By looking at the previous work in the literature, we observe that the most common approach used is supervised learning [20, 38, 12, 21]. In this kind of machine learning, we start from a labeled learning sample (a data set) and define a specific loss function, an objective function measuring the distance between the predicted output and the desired one. The algorithm will adjust the internal model parameters so that the final function minimizes the loss over the known data. Of course, the data set and loss function choices will influence the outcome.

Although databases of experimental measurements and DNS data are readily available, they are only restricted to simple cases which have only limited relevance in more complex problems. Therefore, future work should focus on determining the flow conditions of interest to define the data set. We observe that for the flow studied in the present paper, one could consider a database containing different airfoils and flow configurations. In the RANS results, we observed that the Reynolds number influences the surface's suction and skin friction coefficient peaks. Having a data set composed of only one flow condition would lead to "overfitting", which means that the learned model will be able to minimize the loss function in the training data set, but it will give a high error on unseen data. Besides outlining different flow conditions, model evaluation criteria and error metrics should be defined during the calibration process to avoid model overfitting.

Another point to consider when defining the data set would be the data-model consistency. Suppose machine learning is applied directly to the data. The difference between the learning environment (high fidelity data composing the data set) and the model environment may cause a consistency problem. DNS and LES data may be the best choice in this context since they allow high control of the setup and boundary conditions definition. For example, they may enable excluding possible vortex-tunnel wall interactions and the influence of the probes used to measure the data in the experiments. However, the main drawback of these numerical simulations is their computational cost, posing limitations in the Reynolds number.

Having created a data set, the next step is defining the loss function parameters. The first point is that the more parameters the loss function needs, the more data are required in the training process. Thus the more memory the data set would require. The comparison between the RANS simulations and the experimental data of Chow showed that Linear Eddy Viscosity models could correctly characterize the wing surface flow and the vortical structures' topology. However, they fail to predict the evolution of the mean quantities on the vortex core. The main limitations of the models are the diffusive effect of the turbulent viscosity in the vortex region and the models' specific assumption, which assumes a linear relationship between the Reynold stress tensor and the mean strain rate. Focusing on improving the

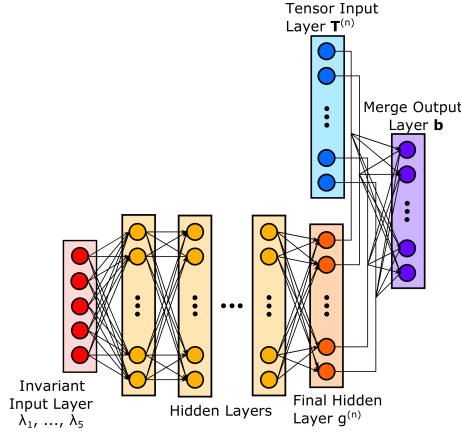


Figure 5.1: Schematic of tensor basis neural network proposed by Ling et al., taken from [20].

capabilities of the turbulence closure on the predictions of persisting non-local anisotropies, given that the invariant tensor components are known from high fidelity simulations, one could use the indicator proposed by Schmitt [35] as a loss function parameter:

$$\rho_{RS} = \frac{|\mathbf{R} : \mathbf{S}|}{\|\mathbf{R}\| \|\mathbf{S}\|} \quad (5.1)$$

where \mathbf{S} is the symmetric part of the velocity gradient tensor and \mathbf{R} are the Reynolds stresses. It should be observed that ρ_{RS} is a measure of the alignment between the two tensors and takes continuous values between 0 and 1. Another possible loss function parameter to use in the training process is the turbulent viscosity ratio. Evidently, a combination of the two loss functions can also be used.

The last points to discuss are the model we would like to improve and the machine learning architecture. Looking at the literature, we observe that an active area of research involves deep learning methods. These are representation-learning methods with multiple levels of representation, obtained by composing simple but non-linear modules that each transform the representation at one level. The main advantage of the technique is the possibility to define complex non-linear parametric models giving high freedom in the definition of the neural network's internal parameters.

In the literature, deep learning methods are implemented following two main approaches. The first is to focus on specific closure components and introduce correction terms that can be learned from the data. For example, Singh and Duraisamy [38] used field inversion in simple neural network architecture to build corrective terms for the Spalart Allmaras model. A spatially varying term $\beta(\mathbf{x})$ is introduced as a multiplier of the production term in the SA equation. The authors observe that the introduction of $\beta(\mathbf{x})$ changes the entire balance between the production and dissipation of turbulent kinetic energy, directly affecting the eddy viscosity prediction. The neural network is defined using β as the model to learn. Following this philosophy, future work could focus on how inverse modeling can improve non-local models, as the Lag-RST model proposed by Olsen and Coakley [28]. The latter takes a baseline two-equation model (as Wilcox's $k - \omega$) and couples it with a third relaxation equation modeling the non-equilibrium effects of the eddy viscosity. In this context, inverse modeling could be used to infer the spatial distribution of model discrepancies and then use deep learning to reconstruct the relaxation equation. The definition of the inverse problem and input features are critical points in this formulation and possible sources of errors.

A second approach is using neural networks to improve Non-Linear Eddy Viscosity models. In this context, we observe that deep learning allows to directly tailor the neural network architecture to satisfy physical and mathematical constraints. As example, Ling et al. [21] developed a deep neural network architecture (Fig.5.1) based on the tensor polynomial decomposition proposed by Pope [30]. The main advantage of this framework is that it directly incorporates Galilean invariance into the tensor predictions. The model would, however, still imply the Boussinesq hypothesis's intrinsic assumption. Therefore, the future work should first analyze the influence of the non-local transport process in the vortex region, which was not possible in the present work.

6

Conclusion

Computations of a wingtip vortex flow were conducted using the open source software SU2 to analyze the accuracy of two Linear Eddy Viscosity turbulence models: the Negative Spalart-Allmaras and the Menter's Shear Stress Transport models. The geometry selected for the study is a NACA-0012 half wing mounted at the wall, with a rounded end cap and trailing edge, inclined by 10° at its quarter chord. Two flow conditions were investigated: $Re = 4.3 \times 10^6$ and $Re = 1.2 \times 10^6$. The computed flow is compared against the experimental data proposed by Chow et al. [7] and the RANS simulations of Churchfield et al. [8] for the first Reynolds number and against the implicit LES simulations predictions of Lombard et al. [23] for the second.

It was found that the Linear Eddy Viscosity models can predict the flow's main topological features. Both SA-NEG and SST models predict the wing tip open separation after about 55% of the chord, as reported in Chow's experiments. Moreover, the visualization of the cross-flow lines combined with the skin friction field clearly shows the presence of two interacting vortical structures in the experimental data. A second vortex is also observed in the cross-flow field downstream of the wing at $x/c = 0.450$, where it causes a deviation of the streamlines, often reported in the literature as vortex "kink".

The presence of the two vortices is associated with two suction regions on the wing surface. Using span-wise cuts, we highlighted the suction and skin friction magnitude peaks related to the two vortices. A higher pressure drop was noted in the wing tip region. Both models predict a surface static pressure distribution in good agreement with the one observed by Chow, with a maximum lift coefficient difference of 11.7% observed in the SA-NEG results. It was also noted that the SST prediction of static pressure profile in the suction region under the vortex at $z/c = -0.023$ is closer to that of the experiment. At lower Reynolds, a clear difference is observed between the RANS and reference LES predictions. The static pressure profile predicted by the first shows a lower peak of the suction region below the primary vortex at $z/c = -0.023$, while in the seconds, we observe a sharp higher suction peak.

The models' vortex centerline location predictions show good agreement with the experimental results. Notably, we observe that the y and z centerline positions computed by the standard SST model are closer to the reference data than the one calculated by Churchfield, using the same model with rotation corrections. However, a substantial discrepancy is observed between the mean quantities evolution in the vortex core computed by the SA-NEG and SST models and the one measured in the experiment. It was noted that this divergence between the numerical simulations and the experimental results is connected to the eddy viscosity, which is three orders of magnitude higher than the physical one in the vortex region and causes a diffusion of the mean quantities. Another consequence of the turbulence viscosity ratio increase is a reduction of the Reynolds stress magnitude downstream of the wing. The SA-NEG and SST models cannot reproduce misalignment with their corresponding strain rate components observed in the experiment.

Although we could not fulfill the project's initial objective, failing to compute the LES simulation of the entire wing, we could still provide indications on possible future work based on comparing the RANS results with the reference experimental and numerical data.

The results show that the Linear Eddy Viscosity models can correctly characterize the flow on the wing surface and the topology of the vortical structures. However, they fail to predict the evolution of the mean quantities on the vortex core. Future work should therefore consider implementing deep

learning strategies to build improved turbulence closure models. Notably, we observed that the tensor basis neural network proposed by Ling et al. [20] could allow the construction of a physical informed architecture that directly embeds the influence of the streamline curvature on the Reynolds stress tensor. Another approach is using the field inversion technique proposed by Parish and Duraisany [12] to infer the spatial distribution of model discrepancies and then use deep learning to reconstruct the relaxation equation of the Lag-RST model [28].

We observed that both suggested approaches are supervised learning methods. Therefore, before considering the implementation of these two deep learning strategies, one should define the data set on which the model is trained and the loss function to minimize. Regarding the high fidelity data, future work should focus on DNS and LES simulation, which allow a high control of the setup. The data set should be constructed considering different flow conditions (angle of attack, Reynolds number) and different airfoil shapes. The first step in this way would be continuing the present work by improving the LES mesh to increase the boundary layer grid definition and obtain a three-dimensional computation around the wing. Comparing the LEVM results against the reference data, we noted that the main limitations of the models are the diffusive effect of the turbulent viscosity in the vortex region and the models' specific assumption. Therefore, possible loss function parameters that can be used are the indicator proposed by Schmitt [35], measuring the alignment between the Reynolds stress and the mean strain rate tensors, and the turbulent viscosity ratio.

References

- [1] S.R. Allmaras, F.T. Johnson, and P.R. Spalart. "Modifications and Clarifications for the Implementation of the Spalart-Allmaras Turbulence Model". In: *7th International Conference on Computational Fluid Dynamics* (9-13 July 2012). url: https://www.iccfd.org/iccfd7/assets/pdf/papers/ICCFD7-1902_paper.pdf.
- [2] R. E. A. Arndt, V. H. Arakeri, and H. Higuchi. "Some observations of tip-vortex cavitation". In: *Journal of Fluid Mechanics* 229 (1991), pp. 269–289.
- [3] J. Boussinesq. "Essai sur la théorie des eaux courantes". In: *Mémoires présentés par divers savants à l'Académie des Sciences XXIII* 1 (1877).
- [4] P. Bradshaw. "Effects of streamline curvature on turbulent flow". In: *AGARDograph* 169 (1973).
- [5] G. T. Chapman. "Topological classification of flow separation on three-dimensional bodies". In: *AIAA Paper* 86-0485 (1986).
- [6] K.-Y. Chien. "Predictions of Channel and Boundary-Layer Flows with a Low-Reynolds-Number Turbulence Model". In: *AIAA Journal* 20.1 (1982), pp. 33–38.
- [7] J. Chow, G. Zilliac, and P. Bradshaw. "Turbulence Measurements in the Near Field of a Wingtip Vortex". In: *NASA technical memorandum* 110418 (1997).
- [8] M. J. Churchfield and G. A. Blaisdell. "Reynolds stress relaxation turbulence modeling applied to a wingtip vortex flow". In: *AIAA Journal* 51 (2013).
- [9] T. Craft et al. "A Computational Study of the Near-Field Generation and Decay of Wingtip Vortices". In: *International Journal of Heat and Fluid Flow* 27 (2006), pp. 684–695.
- [10] J. M. Délery. "Robert Legendre and Henri Werlé: Toward the Elucidation of Three-Dimensional Separation". In: *Annual Review of Fluid Mechanics* 33 (2001), pp. 129–154.
- [11] S. Dong, G.E. Karniadakis, and C. Chrysosostomidis. "A robust and accurate outflow boundary condition for incompressible flow simulations on severely-truncated unbounded domains". In: *Journal of Computational Physics* 261 (2014), pp. 83–105.
- [12] K. Duraisamy E. J. Parish. "A paradigm for data-driven predictive modeling using field inversion and machine learning". In: *Journal of Computational Physics* 305:758–74 (2016).
- [13] M. Giuni. "Formation and early development of wingtip vortices". In: *PhD thesis* (2013).
- [14] M. Giuni and E. Benard. "Analytical/Experimental Comparison of the Axial Velocity in Trailing Vortices". In: *American Institute of Aeronautics and Astronautics* (2011).
- [15] M. Giuni and R. B. Green. "Vortex formation on squared and rounded tip". In: *Aerospace Science and Technology* 29 (2013), pp. 191–199.
- [16] T. L. Grow. "Effect of a wing on Its Tip Vortex". In: *Journal of Aircraft* 6.1 (1969), pp. 37–41.
- [17] A. Guardone, D. Isola, and G. Quaranta. "Arbitrary Lagrangian Eulerian formulation for two-dimensional flows using dynamic meshes with edge swapping". In: *Journal of Computational Physics* 230 (2011), pp. 7706–7722.
- [18] K. Hillewaert. "The discontinuous Galerkin method. A practical introduction." In: *internal note* (2022).
- [19] M. J. Lighthill. *Laminar Boundary Layer Theory*. L. Rosenhead. Oxford University Press, 2000, pp. 72–82.
- [20] J. Ling and J. Templeton. "Evaluation of machine learning algorithms for prediction of regions of high Reynolds averaged Navier Stokes uncertainty". In: *Physics of Fluids* 27:085103 (2015).
- [21] J. Ling and J. Templeton. "Reynolds Averaged Turbulence Modeling using Deep Neural Networks with Embedded Invariance". In: *Journal of Fluid Mechanics* 807 (2016), pp. 155–166.

- [22] T. Liu. "Global skin friction measurements and interpretation". In: *Progress in Aerospace Sciences* 111.100584 (2019).
- [23] J. W. Lombard et al. "Implicit Large Eddy Simulation of a wingtip vortex at $Re_c = 1.2 \times 10^6$ ". In: *AIAA Journal* 110418 (2015). doi: 10.2514/1.J054181.
- [24] K. W. McAlister and R. K. Takahashi. "Avscom technical report 91-a-003 naca 0015 wing pressure and trailing vortex measurement". In: *Nasa Technical Paper* 3151 (1991).
- [25] F.R. Menter. "Two-Equation Eddy-Viscosity Turbulence Models for Engineering Applications". In: *AIAA Journal* 32.8 (1994), pp. 1598–1605.
- [26] R. Nichols. "Algorithm and Turbulence Model Requirements for Simulating Vortical Flows". In: *AIAA Paper* 2008-0337 (2008).
- [27] S. Nisizima and A. Yoshizawa. "Turbulent channel and Couette flows using a anisotropic k-mode". In: *AIAA Journal* 25 (1986), pp. 414–420.
- [28] M. Olsen and T. Coakley. "The Lag Model, a Turbulence Model for Non Equilibrium Flows". In: *AIAA 15th Computational Fluid Dynamics Conference* AIAA Paper 2001-2564 (2001).
- [29] *Osborne Reynolds Centenary volume*. A 451. 1–318. London: Proc. R. Soc. London, 1995.
- [30] S. B. Pope. "A more general effective-viscosity hypothesis". In: *Journal of Fluid Mechanics* 72 (1975), pp. 331–340.
- [31] Stephen B. Pope. *Turbulent Flows*. Cambridge University Press, 2000, pp. 359–365.
- [32] L. Prandtl. "Über Flüssigkeitsbewegung bei sehr kleiner Reibu". In: *Verh. III, Int. Math. Kongr., Heidelberg*, 27 (1904), pp. 484–491.
- [33] V. J. Rossow et al. "Wind-tunnel measurements of hazard posed by lift-generated wakes". In: *Journal of Aircraft* 32 (1995), pp. 278–284.
- [34] T. Sarpkaya. "Decay of vortices of large aircraft". In: *Proceeding of the 36th Aerospace Sciences Meeting Exhibit* (1998).
- [35] F.G. Schmitt. "About Boussinesq's turbulent viscosity hypothesis: historical remarks and a direct evaluation of its validity". In: *Comptes Rendus Mécanique* 335 (2007), pp. 9–10.
- [36] M. L. Shur et al. "Turbulence Modeling in Rotating and Curved Channels: Assessing the Spalart-Shur Correction". In: *AIAA Journal* 38.5 (2000), pp. 784–792.
- [37] R. L. Simpson. "Aspects of turbulent boundary layer separation". In: *Progress in Aerospace Science* 32 (1996), pp. 457–521.
- [38] A. P. Singh, S. Medida, and K. Duraisamy. "Machine-learning-augmented predictive modeling of turbulent separated flows over airfoils". In: *AIAA Journal* 55:2215–27 (2017).
- [39] J. Smahorinsky. "General Circulation Experiments With The Primitive Equations". In: *Monthly Weather Review* 91.3 (1963).
- [40] P.E. Smirnov and F.R. Menter. "Sensitization of the SST Turbulence Model to Rotation and Curvature by Applying the Spalart-Shur Correction Term". In: *ASME Journal of Turbomachinery* 131 (2009).
- [41] P.R. Spalart and S.R. Allmaras. "A One-Equation Turbulence Model for Aerodynamic Flows". In: *Recherche Aerospatiale* 1 (1994), pp. 5–21.
- [42] C.G. Speziale. "On nonlinear k-l and k-epsilon models of turbulence". In: *Journal of Fluid Mechanics* 178 (1987), pp. 459–475.
- [43] *SU2code*. 2022. url: <https://su2code.github.io/> (visited on 08/22/2022).
- [44] D. Sujundi and R. Haimes. "Identification of Swirling Flow in 3-D Vector Fields". In: *AIAA paper* 95-1715 (1995).
- [45] V. Terrapon. *AERO0004 - turbulent flows*. 2022. url: https://www.mtfc.uliege.be/cms/c_4048443/en/mtfc-teaching (visited on 06/28/2022).
- [46] D. H. Thompson. "A Flow Visualization Study of Tip Vortex Formation". In: *ARL-Aero-Note* 421 (1983).

- [47] M. Tobak and D. J. Peake. "Topology of three-dimensional separated flows". In: *Annual Review of Fluid Mechanics* 14 (1982), pp. 61–85.
- [48] *Visual Computing Group - Hiedelberg University*. 2022. url: https://vcg.iwr.uni-heidelberg.de/plugins/vcg_-_vortex_core_lines (visited on 08/22/2022).
- [49] S. Vitale et al. "Extension of the SU2 open source CFD code to the simulation of turbulent flows of fluids modelled with complex thermophysical laws". In: *22nd AIAA Computational Fluid Dynamics Conference* (2015).
- [50] K. C. Wang. "Separation of three-dimensional flow". In: *Review in Viscous Flow, Proc. Lockheed-Georgia Co. Symp.* LG 77ER0044 (1976), pp. 341–414.
- [51] D.C. Wilcox. "Reassessment of the Scale-Determining Equation for Advanced Turbulence Models". In: *AIAA Journal* 26.11 (1988), pp. 1299–1310.
- [52] B. A. Younis, T. B. Gatski, and C. G. Speziale. "Towards a rational model for the triple velocity correlations of turbulence". In: *Proceedings of the Royal Society of London A: Mathematical, Physical and Engineering Sciences* 456.1996 (2000), pp. 909–920.